

# Laser–solid interaction studies enabled by the new capabilities of the iP2 BELLA PW beamline

Cite as: Phys. Plasmas **29**, 083102 (2022); <https://doi.org/10.1063/5.0089331>

Submitted: 24 February 2022 • Accepted: 30 June 2022 • Published Online: 19 August 2022

 Sahel Hakimi,  Lieselotte Obst-Huebl,  Axel Huebl, et al.

## COLLECTIONS

Paper published as part of the special topic on [Papers from the 63rd Annual Meeting of the APS Division of Plasma Physics](#)



View Online



Export Citation



CrossMark

## ARTICLES YOU MAY BE INTERESTED IN

[Meter-scale plasma waveguides for multi-GeV laser wakefield acceleration](#)

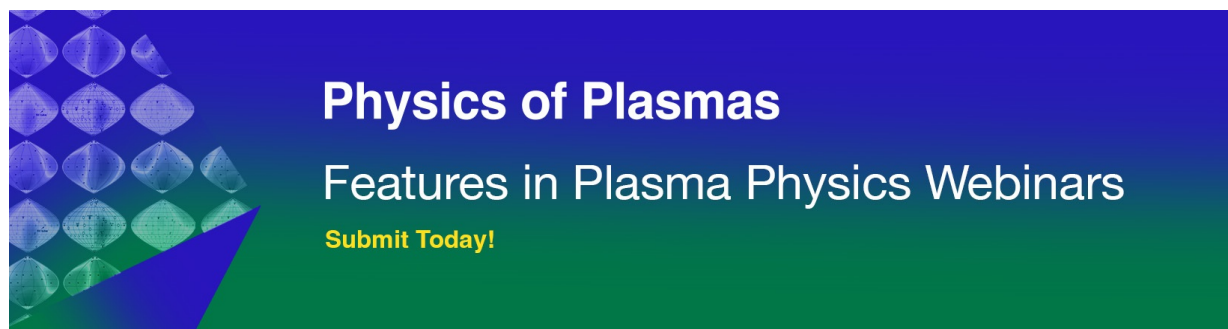
Phys. Plasmas **29**, 073101 (2022); <https://doi.org/10.1063/5.0097214>

[Relativistic plasma physics in supercritical fields](#)

Phys. Plasmas **27**, 050601 (2020); <https://doi.org/10.1063/1.5144449>

[Ion acceleration in laser generated megatesla magnetic vortex](#)

Phys. Plasmas **26**, 103108 (2019); <https://doi.org/10.1063/1.5094045>



# Laser-solid interaction studies enabled by the new capabilities of the iP2 BELLA PW beamline

Cite as: Phys. Plasmas **29**, 083102 (2022); doi: [10.1063/5.0089331](https://doi.org/10.1063/5.0089331)

Submitted: 24 February 2022 · Accepted: 30 June 2022 ·

Published Online: 19 August 2022



View Online



Export Citation



CrossMark

Sahel Hakimi,<sup>a)</sup> Lieselotte Obst-Huebl,<sup>b)</sup> Axel Huebl,<sup>c)</sup> Kei Nakamura,<sup>d)</sup> Stepan S. Bulanov,<sup>e)</sup> Sven Steinke,<sup>f)</sup> Wim P. Leemans,<sup>g)</sup> Zachary Kober,<sup>h)</sup> Tobias M. Ostermayr,<sup>i)</sup> Thomas Schenkel,<sup>j)</sup> Anthony J. Gonsalves,<sup>k)</sup> Jean-Luc Vay,<sup>l)</sup> Jeroen van Tilborg,<sup>m)</sup> Csaba Toth,<sup>n)</sup> Carl B. Schroeder,<sup>o)</sup> Eric Esarey, and Cameron G. R. Geddes<sup>p)</sup>

## AFFILIATIONS

Lawrence Berkeley National Laboratory, Berkeley, California 94720, USA

**Note:** This paper is part of the Special Collection: Papers from the 63rd Annual Meeting of the APS Division of Plasma Physics.

**Note:** Paper C11 4, Bull. Am. Phys. Soc. **66** (2021).

<sup>a)</sup> Author to whom correspondence should be addressed: [sahelh@lbl.gov](mailto:sahelh@lbl.gov)

<sup>b)</sup> Invited speaker.

<sup>c)</sup> Present address: Marvel Fusion GmbH, Blumenstrasse 28, 80331 München, Germany.

<sup>d)</sup> Present address: Deutsches Elektronen-Synchrotron (DESY), Notkestrasse 85, 22607 Hamburg, Germany.

<sup>e)</sup> Also at: Department of Nuclear Engineering, University of California, Berkeley, California 94720, USA.

<sup>f)</sup> Electronic mail: [cgrgeddes@lbl.gov](mailto:cgrgeddes@lbl.gov)

## ABSTRACT

The new capabilities of the short focal length, high intensity beamline, named iP2, at the BELLA Center will extend the reach of research in high energy density science, including accessing new regimes of high gradient ion acceleration and their applications. This 1 Hz system will provide an on-target peak intensity beyond  $10^{21}$  W/cm<sup>2</sup> with a temporal contrast ratio of  $<10^{-14}$  that will be enabled by the addition of an on-demand double plasma mirror setup. An overview of the beamline design and the main available diagnostics are presented in this paper as well as a selection of accessible research areas. As a demonstration of the iP2 beamline's capabilities, we present 3D particle-in-cell simulations of ion acceleration in the magnetic vortex acceleration regime. The simulations were performed with pure hydrogen targets and multi-species targets. Proton beams with energy up to 125 MeV and an approximately 12° full angle emission are observed as preplasma scale length and target tilt are varied. The number of accelerated protons is on the order of  $10^9$ /MeV/sr for energies above 60 MeV.

Published under an exclusive license by AIP Publishing. <https://doi.org/10.1063/5.0089331>

## I. INTRODUCTION

Laser-driven plasma accelerators<sup>1–4</sup> are attractive alternatives to conventional accelerators in order to reduce the size and cost, and therefore, increase the availability of accelerators for a variety of applications. It is known that the interaction of an intense laser pulse with solid-density targets can generate energetic ion beams via several different mechanisms depending on the laser and target parameters.<sup>2,3,5</sup> Laser-accelerated ion pulses hold unique properties, including a high particle number of various ion species (up to  $10^{13}$  particles per pulse), short pulse duration (picoseconds at the source), and low emittance (below 0.004 mm mrad).<sup>6</sup> These are in addition to the localized energy deposition of ion beams due to the Bragg peak phenomenon in the case of a monoenergetic beam or an energy selecting/chromatic beamline. They are, therefore, of interest for applications such as hadron

therapy,<sup>7</sup> fusion ignition,<sup>8</sup> radiography,<sup>9</sup> and warm dense matter studies.<sup>10</sup>

In order to realize the potential applications of laser-driven ion beams, improvements in beam parameters such as maximum energy, number of accelerated ions, and beam divergence are required as well as a stable and reliable operation at high repetition rates. For example, particular interest was recently sparked in radiotherapy with ultra-high dose rates, where the FLASH radiotherapy effect (see Ref. 11 and references therein) can induce differential normal tissue sparing without significant changes to the therapeutic tumor response. Laser-accelerated proton beams feature uniquely high instantaneous dose rates, and it was demonstrated that differential normal tissue sparing was indeed induced when irradiating normal cells and tumor cells *in vitro*.<sup>12</sup> Advancing to *in vivo* studies requires several tens of MeV

proton energies in order to penetrate deeper into the tissue of small animal tumor models, and ultimately, proton energies exceeding 100 MeV are required for laser-driven proton therapy in humans. Proton energies exceeding 100 MeV from a laser-driven proton source are yet to be demonstrated. Moreover, a sophisticated proton transport beamline is necessary to capture and transport the generated proton pulses to a dedicated irradiation site and to apply a homogeneous lateral and depth dose profile to the tumor.<sup>13</sup>

Laser-driven ion acceleration mechanisms include Target Normal Sheath Acceleration (TNSA),<sup>14</sup> Coulomb Explosion (CE),<sup>15,16</sup> Radiation Pressure Acceleration (RPA),<sup>17</sup> Shock Acceleration (SA),<sup>18,19</sup> and Magnetic Vortex Acceleration (MVA).<sup>20–22</sup> TNSA poses less stringent requirements to laser and target conditions than the other mechanisms and has therefore been most widely studied in experiments. In TNSA, ion energy scales as  $\sqrt{P_L}$ , where  $P_L$  is the laser power. To date, a maximum proton energy of 85 MeV has been reported from TNSA experiments.<sup>23,24</sup> Advanced mechanisms,<sup>5</sup> such as RPA and MVA, require ultra-high intensity and ultra-high contrast pulses, and therefore, have proven to be more challenging to reach in experiments. Although initial exploration of these regimes has begun,<sup>25–33</sup> their full potential has not yet been realized. These mechanisms promise a higher laser to ion energy conversion efficiency and better energy scaling to reach hundreds of MeV to GeV per nucleon energies as predicted by numerical simulations.<sup>34,35</sup> MVA also promises reduced emission angles of approximately  $10^\circ$ , which would facilitate subsequent capture and transport to an irradiation site. The MVA mechanism differs from the other mechanisms mainly due to the fact that laser propagation in Near-Critical Density (NCD) targets of tens of  $\mu\text{m}$  thickness, sets up an azimuthal magnetic field in the self-generated density channel behind the laser. Subsequently, ion acceleration occurs during the expansion of this magnetic field, after it exits the target rear. Theoretically, ion energy scales as  $P_L^{2/3}$  for the MVA regime.<sup>35</sup> Figure 1 shows examples of theoretical scaling laws<sup>34,35</sup> for proton energy vs laser intensity.

A collection of experimental data on maximum proton energy achieved to date is presented in Fig. 1 with energies approaching 100 MeV (Refs. 28 and 29) from a TNSA-RPA hybrid scheme. These experiments are conducted at different facilities, which operate with laser energies ranging from a few to hundreds of Joules, pulse durations ranging from tens of fs to hundreds of ps, focal spot sizes of a few to tens of  $\mu\text{m}$ , and unique temporal intensity profiles, producing ion beams with varying maximum energies. In some cases, produced ion beams from facilities with similar capabilities seem to differ as well, which may be due to unknown parameters in the models, varying diagnostics implemented, or the lack of control over the non-linear dynamics, for example, target expansion. The majority of these experiments are conducted in the TNSA regime, while experimental investigation of advanced mechanisms is less frequent due to more stringent requirements of laser and target parameters as mentioned above. Further experiments should be conducted targeting these regimes to study the microscopic physics involving target heating, plasma formation, and laser energy absorption and realize ion beam parameters required for the foreseen applications.

The new iP2 beamline addition to the 1 Hz BELLA PW laser will provide the necessary ultra-high intensity and ultra-high temporal contrast to systematically study advanced ion acceleration mechanisms, such as RPA and MVA, at high repetition rates. Previously,

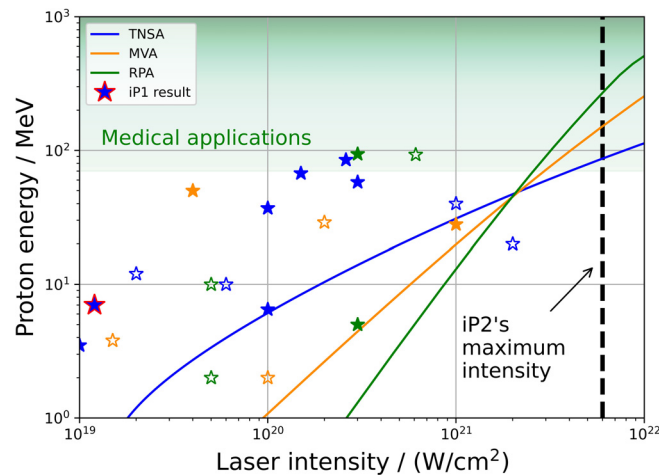


**FIG. 1.** Scaling laws for different acceleration mechanisms are shown for a pulse duration of  $\sim 35$  fs. A collection of experimental data on maximum observed proton energies at various laser intensities is shown (from Ref. 34 and references therein and Ref. 36). Experiments in the TNSA regime are shown in blue, and experiments reporting on the onset of advanced mechanisms are shown in green. Result of the previous experiment using the BELLA PW is shown (blue/red star). Previous experiments conducted with NCD targets<sup>31,32,37–39</sup> are highlighted in orange. Experiments conducted with a pulse duration of  $< 50$  fs are shown with hollow stars. The range of proton energies relevant to medical applications is displayed in green. The maximum on-target peak intensity of the iP2 beamline is marked with a dashed black line.

TNSA experiments with the BELLA PW laser have produced high charge, low divergence ion beams with cutoff energies around 8 MeV (Ref. 40) at  $10^{19} \text{ W/cm}^2$ . This is marked as iP1 result in Fig. 1. The iP2 beamline with its short focal length focusing optic will provide an on-target peak intensity beyond  $10^{21} \text{ W/cm}^2$  with an ultra-high temporal contrast ratio of  $< 10^{-14}$ , to be enabled by the addition of an on-demand double plasma mirror (DPM) setup. Importantly, this new beamline will operate in the intensity regime where scaling laws intersect, as shown in Fig. 1, and can therefore be a platform to study transitions between acceleration mechanisms with consistent laser parameters and diagnostics across experiments. This will provide a reliable comparison of ion beam characteristics from different regimes and eliminate uncertainties due to variables in the facility parameters and operation, potentially identifying which regime is best suited for a particular application. The 1 Hz repetition rate of the BELLA PW, when paired with a suitable high repetition rate targetry system and diagnostics, allows for large parameter scans at statistical relevance to explore different laser and target conditions for the various acceleration regimes. Furthermore, machine learning algorithms can be implemented to optimize ion beam characteristics.

The laser pulses generated in PW-class laser systems are usually accompanied by a pedestal of nanosecond duration and short prepulses on various time scales. This portion of the pulse can be focused to intensities above the damage threshold of the target material and as such it can heat, ionize, and expand the target. Among other effects,<sup>41</sup> this can result in formation of a preplasma on the front and rear sides of the target and alter the target profile prior to the arrival of the main pulse.<sup>42</sup> The motion of fast electrons and soft x-rays through the target, thermal conduction, and shock wave propagation in the target can

contribute to the heating of the rear surface.<sup>43</sup> In order to prepare for upcoming experiments at iP2 and showcase the facility's capabilities, we investigate the robustness and performance of MVA under varied density ramps with particle-in-cell (PIC) simulations to study acceleration conditions with and without laser contrast cleaning. For the MVA mechanism, the evolution of the magnetic field at the target rear depends on how the plasma density varies and affects the acceleration process. The direction and collimation of ion beams in the case of an off-normal angle of incidence are studied, identifying potentially observable signatures in experiments. Simulations are performed with pure hydrogen and mixed targets to investigate multi-species effects.

The rest of this paper is organized as follows: Sec. II provides details of the laser system and an overview of the newly constructed iP2 beamline and chamber as well as the main planned diagnostics. A summary of research areas of interest is provided in Sec. III. Section IV describes the simulation setup and presents the results followed by concluding remarks in Sec. V.

## II. FACILITY CAPABILITY AND BEAMLINE PARAMETERS

### A. Laser system

The BELLA Center houses four main laser systems: the BELLA PW laser system,<sup>44</sup> two 100-TW (HTW) laser systems,<sup>45,46</sup> and a commercial TW, kHz system. The 1 Hz BELLA PW laser, one of the world's highest repetition rate PW-class lasers, has been operational since 2013, delivering up to 40 J in 35 fs, mainly for high energy electron and ion acceleration experiments.<sup>40,47,48</sup> The BELLA PW laser has also been a part of LaserNetUS<sup>49</sup> since its first cycle, providing beamtime for a variety of experiments including plasma mirror experiments.<sup>50</sup> A detailed discussion of the BELLA PW laser parameters including both spatial and temporal properties is given in Ref. 44. Full spatio-temporal time-resolved measurements in both the near and far-field of the laser pulses at >1 PW peak power have also been previously studied.<sup>51,52</sup>

### B. Beamlines

The layout of the BELLA PW laser and the experimental area, housing two separate chambers, are shown in Fig. 2. The original BELLA PW beamline is focused at the upstream side of the target chamber 1 with an  $f/65$  off-axis parabolic (OAP) mirror. This beamline can reach a maximum on-target peak intensity of  $I = 1.2 \times 10^{19}$  W/cm<sup>2</sup>. A recent upgrade was the construction of a second beamline, independently tunable, which will enable staged acceleration<sup>53</sup> of multi-GeV electron beams.<sup>54</sup> This second beamline is split from the main beamline before compression, and the two beams will deliver a total energy of up to 40 J for electron and ion acceleration studies and staging experiments in target chamber 1.

In parallel, a high intensity beamline,<sup>55</sup> named iP2 (short for interaction point 2), was added to the system with a short focal length focusing optic and a separate target chamber, dedicated to experiments at ultra-high intensity and temporal contrast, such as laser–solid interactions. The new iP2 beamline is an extension to the existing BELLA PW laser with an on-demand DPM setup foreseen in the target chamber 1 to clean the laser pulse from preceding prepulses and pedestals. After reflecting off the two plasma mirrors, the diverging beam will be routed toward a long focal length OAP, which re-collimates the beam and sends it to the iP2 chamber, where the beam will be focused to a spot size of a few micrometer with a short focal length ( $f/2.5$ ) OAP.

Focal spot measurements conducted with the 150  $\mu$ J beam from the booster amplifier<sup>44</sup> show a beam profile with a FWHM of 2.8 and 3.1  $\mu$ m in the horizontal and vertical directions. The wavefront error of the BELLA PW beamline at high power was reported to be  $40 \pm 10$  nm (Ref. 44), while recent measurements at low power indicate a wavefront error of  $46 \pm 10$  nm. Thus, it is reasonable to expect the fluence profile in Fig. 2 to be a good approximation to that of the full BELLA PW energy of 40 J. In this case, the peak intensity is expected to be  $6 \times 10^{21}$  W/cm<sup>2</sup>. Therefore, this beamline will deliver peak intensities beyond  $I = 1 \times 10^{21}$  W/cm<sup>2</sup> in target chamber 2 (iP2 chamber) for ultra-high intensity interactions. The angular fluctuation of the beam for the long focal length system was reported to be 1.3  $\mu$ rad,<sup>44</sup> which translates to  $\sim 18$   $\mu$ m pointing stability. The angular fluctuation is expected to be at a similar level for the iP2 beamline, giving a pointing fluctuation on the order of 1  $\mu$ m. In the future, a  $\lambda/4$  waveplate will be added to the beamline in order to switch between linear and circular polarization on-demand to explore ion acceleration dependence on laser polarization.

The DPM will initially be realized by using fused silica substrates with anti-reflective coatings on both front and rear sides. Later, high repetition rate capable plasma mirror technologies, such as liquid crystal films,<sup>56</sup> will be fielded. Previous experiments with plasma mirrors at the BELLA PW give reason to believe more than 70% of the initial laser energy could be reflected from the DPM system while providing significant contrast improvement.<sup>57,58</sup> Until it is measured during commissioning experiments, we will assume a more conservative total reflectivity of 60% for planning purposes. Thus, of an initial 40 J laser pulse, at least 24 J will be available for experiments in the iP2 chamber when using the DPM.

### C. Planned diagnostics

Laser beam properties (spectral, spatial, and temporal) can be measured at full power using a high power diagnostics suite before entering the iP2 chamber. This includes near and far-field diagnostics of the laser mode, a wavefront sensor, a third-order autocorrelator (Sequoia), self-referenced spectral interferometry (WIZZLER), frequency-resolved optical gating (FROG), ns-prepulse monitoring, and a broadband optical spectrometer. The temporally integrated intensity distribution and wavefront in the iP2 focus can be measured at low power, where the fully amplified laser pulse is attenuated before compression via reflection from three uncoated wedges. The focal spot mode can be optimized with a deformable mirror located after the final amplification. Laser operation, diagnostics control, and data collection are managed with the distributed control system GEECs (generalized equipment and experiment control systems).<sup>59</sup> This system also allows for fully automated parameter scanning, data plotting, and analysis. The thoroughly characterized laser pulses will be delivered to the target with flexible experimental arrangements and diagnostics. The iP2 chamber allows for varying laser incidence angles on the target. Initial experiments will be conducted with  $\theta = 0^\circ$  and  $24^\circ$  incidence angles. The main diagnostics planned for accelerated ion beams at iP2 are a Thomson parabola spectrometer (TPS) with an active microchannel plate (MCP), a phosphor screen and a CCD, and passive radiochromic film (RCF) stacks, which are both briefly explained in the following two sections. Further dedicated diagnostics of the laser–plasma interactions, such as measurements of the reflected and transmitted laser pulse remnant, the emitted hot



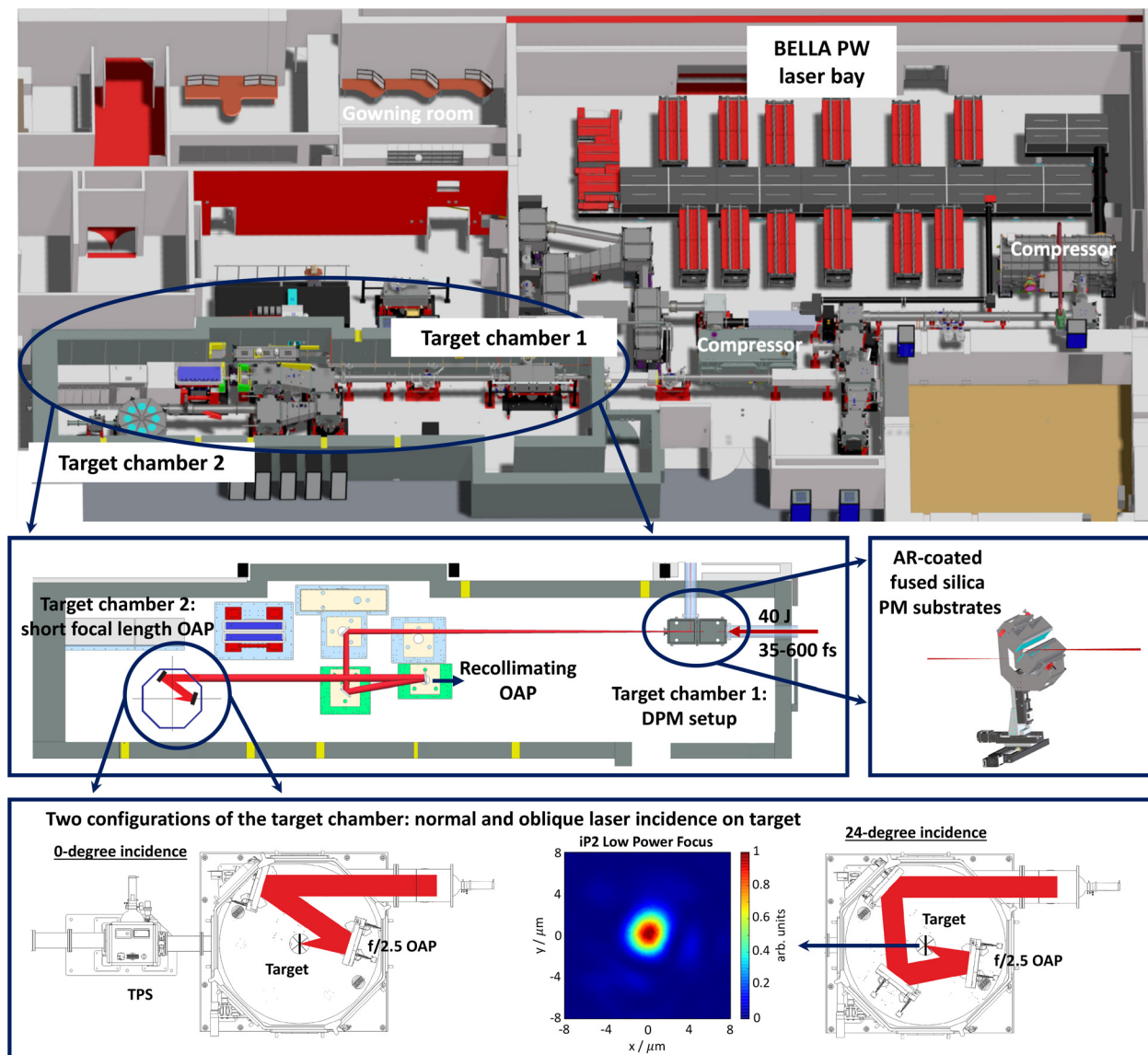


**FIG. 2.** Layout of the BELLA PW laser and the experimental area. An on-demand double plasma mirror will be available in the target chamber 1 for temporal pulse contrast cleaning. The beam is then re-collimated before entering the target chamber 2, housing an  $f/2.5$  off-axis parabolic mirror for the final focusing. Different laser incidence angles on target can be realized. Here, two possible configurations of  $0^\circ$  and  $24^\circ$  incidence angle are displayed. A Thomson parabola spectrometer equipped with a microchannel plate and a phosphor screen is located in a separate, differentially pumped vacuum chamber. A measurement of the iP2 focal spot conducted with the booster amplifier output of  $150\ \mu\text{J}$  and normalized to the peak value is shown.

electrons and x-rays, and the plasma density profile via optical probing, will be fielded for experiments.

### 1. Thomson parabola spectrometer

In order to measure the spectra of ion species with different charge-to-mass ratios, a Thomson parabola spectrometer (TPS) equipped with an MCP followed by a phosphor screen that is imaged to a CCD will be used. A TPS allows for the detection of ion energy spectra in a small portion of the beam, sampled with a pinhole. An electric field

separates the different ion species depending on their charge-to-mass ratio, and a parallel (or anti-parallel) magnetic field deflects the ions according to the Lorentz force. This results in parabolic traces on a detector positioned at a certain drift distance after the electric and magnetic fields. The energetic ions with higher velocities will be deflected less; therefore, a longer drift is needed to obtain a good resolution at higher energies.

The TPS design for iP2 includes a separate and differentially pumped vacuum chamber, which houses the electric plates, dipole magnet, and MCP/phosphor screen assembly for 1 Hz repetition rate

operation. The phosphor screen is imaged to a CCD camera outside the chamber. As iP2 will be used for investigation of advanced acceleration schemes to reach higher ion energies, as predicted by numerical simulations discussed in Sec. IV, the TPS geometry is designed to detect up to 100 MeV protons. A pinhole with a diameter between 100 and 500  $\mu\text{m}$  in a 1.5 cm thick stainless steel block, enough to shield a 100 MeV proton beam, is positioned 0.73 m behind the target and along the ion beam axis. A second collimator with a 5 mm diameter and the same thickness and material is placed inside the vacuum tube between the two chambers. The electric field strength is 800 kV/m over a length of 150 mm. The magnetic field inside the dipole assembly is constant at  $B = 0.264$  T, confirmed by Hall probe measurements, and has an effective length of 275.2 mm. The drift distance to the MCP screen is approximately 0.5 m. This TPS geometry provides a reasonable low energy cutoff and a good resolution at the expected maximum energy. In addition, employing pinholes of different sizes allows for absolute particle number measurements at different energies. Figure 3(a) shows the deflection of various ion species in the detector plane for this geometry with the energy-dependent resolution given in Fig. 3(b) for a 400  $\mu\text{m}$  diameter pinhole. The shaded region in Fig. 3(a) displays the active area of the MCP with a 96 mm diameter. The center of the MCP is shifted with respect to the ion beam axes

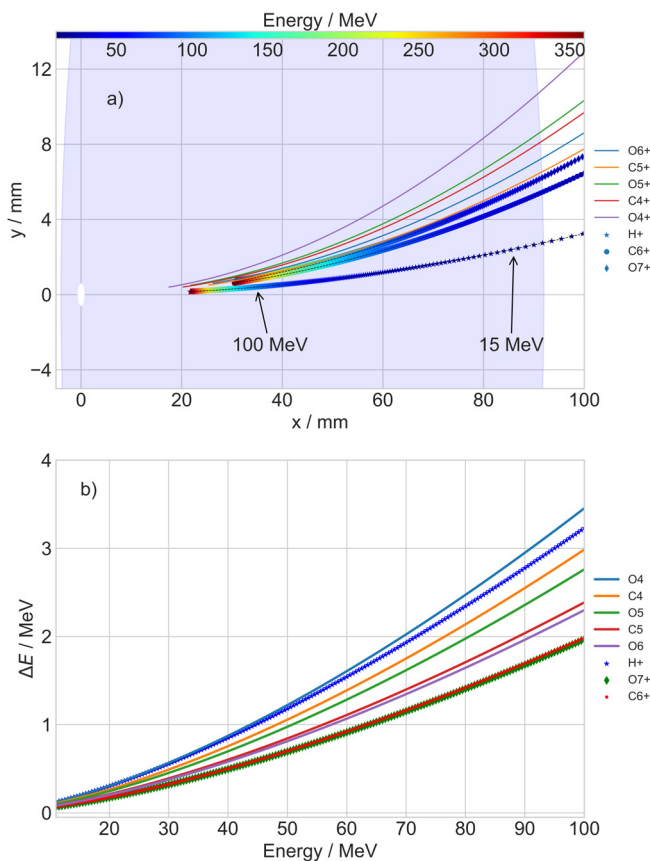


**FIG. 3.** (a) Deflection of ion species in the detector plane and (b) the energy-dependent resolution with a 400  $\mu\text{m}$  diameter pinhole based on analytical calculations.

such that the neutral spot, shown in white, is located a few millimeters from the edge. Ions are plotted in the 10–360 MeV kinetic energy range, a decision informed by simulations. The low energy cutoff for protons is between 10 and 20 MeV depending on the exact positioning of the components. The energy resolution is mainly limited by the size of the ion beam on the MCP corresponding to the projection of the pinhole size on the MCP plane. For this design, the energy resolution is 3.2% for a proton energy of 100 MeV. With a 200  $\mu\text{m}$  diameter pinhole, the proton trace (up to 100 MeV) is distinguishable from heavier ions with a reasonable signal to noise as long as their energy is less than 360 MeV. Optimizing between the energy resolution and sufficient particle numbers while maintaining a reasonable low energy cutoff at the MCP resulted in the current TPS design. In general, the design is flexible, and variations in the drift distance and aperture size are possible in order to increase the resolution at the high energy tail of the spectra at the expense of not detecting the lower energy ions. The activation of multiple MCP channels due to the increased penetration depths of higher ion energies needs to be taken into account for spectral evaluation of the generated traces.

## 2. Radiochromic film stacks

In addition to the TPS that allows for the spectral characterization of a portion of the ion beam sampled with a pinhole, calibrated self-developing radiochromic films (RCFs) will be used for selected shots to measure the absolute proton number and the angular proton emission distribution.<sup>60</sup> After proton exposure, the films need to be scanned, and the changes in their optical density need to be analyzed in order to draw quantitative conclusions. RCFs will be used in stack configuration, where different penetration depths in a stack correspond to different energy classes in the proton beam. In order to detect up to 100 MeV protons, metal absorbers will be interleaved with RCFs to achieve a reasonable energy resolution while maintaining a manageable stack thickness and weight. Rigorous unfolding of the proton spectra requires Monte Carlo simulations to derive the deposited energy of the different incoming proton energy classes in the sensitive layers of the RCF stack.<sup>61</sup> For iP2, we have designed stacks with an energy resolution of about 5 MeV. Up to seven stacks can be mounted on a motorized wheel and moved into the proton beam on selected shots during the experiment. Loading the wheel with a new set of stacks requires venting the vacuum chamber.

We performed Monte Carlo simulations with SRIM<sup>62</sup> and TOPAS<sup>63</sup> to design plausible stack configurations for the predicted proton energy range at iP2 and to prepare for future spectral unfolding and data analysis. The RCF material parameters were drawn from Ref. 64. While both SRIM and TOPAS perform 3D simulations and account for off-axis scattering, TOPAS allows for fully arbitrary 3D input beams and target designs, whereas SRIM can only model collimated input beams with flat transverse profiles. We expect proton emission angles on the order of tens of degrees depending on proton energy and the dominating acceleration mechanism. Thus, accurate modeling of diverging beams in these fairly thick film stacks is important due to the increased effects of path length differences and scattering. Figure 4 shows the linear energy transfer (LET) profiles simulated with SRIM and TOPAS for the 100 MeV RCF stack for different input energies and emission characteristics. When comparing SRIM and TOPAS for a collimated 100 MeV beam, differences in LET in the

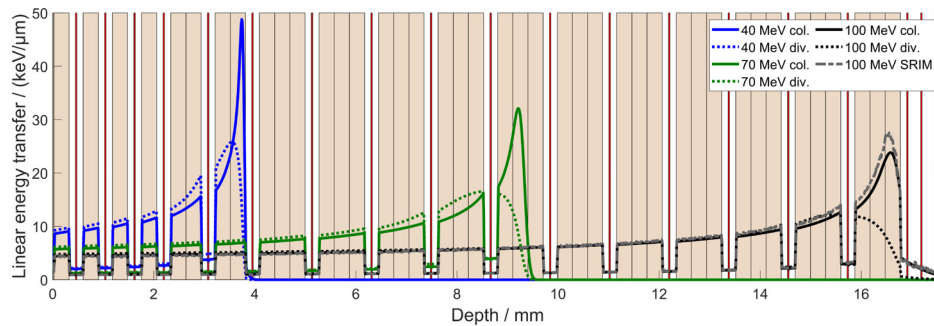


**FIG. 4.** Radiochromic film stack design and Monte Carlo simulation results for proton stopping in the stack. This stack is made up of 300  $\mu\text{m}$  copper absorbers (beige) and EBT-3 RCF (Gafchromic, sensitive layer is shown in red, substrate layer in white). Linear energy transfer profiles are from TOPAS simulations with the exception of the gray dashed curve, which is from a SRIM simulation. Input proton energies of 40 MeV (blue), 70 MeV (green), and 100 MeV (black/gray) for collimated (solid) and diverging (dotted, Gaussian angle distribution with  $15^\circ$  standard deviation) beams are shown. SRIM only allows for collimated input beams. Protons and ions deposit most of their energy at the end of their track in the Bragg peak before being fully stopped.

sensitive layers of the RCF are at most 7%, which is consistent with slightly different physics models and databases used between the two codes. Comparing the LET profiles of collimated vs diverging beams (Gaussian angle distribution with  $15^\circ$  standard deviation) with TOPAS, variations are visible in the Bragg peak regions of the different energy classes investigated here. The Bragg peak broadening in the case of diverging input beams is the result of path length differences and particle loss due to increased lateral momenta from scattering. The difference of LET in the sensitive layers of the RCF amounts to a maximum of 10% when considering the region before the diverging beam is stopped, which is earlier than for the collimated beam case.

TOPAS also allows for simulation of secondary particle production upon proton impact on the stack and their contribution to the overall deposited energy in the RCF. For the 100 MeV stack design with interleaved copper absorbers, secondary particles can add up to 10% of deposited energy in the sensitive layers of RCFs. The more realistic simulated data from TOPAS provides a better description of the divergence and LET at each active layer of RCF across multiple energies and will translate into a more accurate spectral analysis of the proton beams generated at iP2.

### III. FOCUS AREAS OF RESEARCH

In addition to investigating ion acceleration via advanced mechanisms and use of novel targets, iP2 is suited to study fundamental relativistic plasma phenomena taking place on the micrometer and the femtosecond scale, high harmonic generation from overcritical density targets requiring extremely clean pulses in the short pulse regime, principle concepts related to inertial fusion energy studies, and multi-disciplinary applications enabled by high charge, multi-species, laser-driven ion beams.

These ultra-relativistic laser–solid interactions feature extreme conditions, enabling discovery science studies in high energy density science (HEDS) and warm dense matter (WDM) research, for example, by creating temperatures and pressures present in astrophysical objects on the laboratory scale, or by generating strong shocks and hydrodynamic instabilities. Different regimes of these phenomena could be driven either by the relativistic laser pulse itself or by the laser-accelerated ion beams. The latter are particularly suited to isochorically heat solid density material to the WDM state. Due to the

high energy density and short temporal duration of these ion beams, heating can occur uniformly and on a picosecond time scale before matter expands hydrodynamically.

Strong Field Quantum Electrodynamics (SFQED) effects that start to manifest themselves in laser-charged particle interactions at ultra-high intensities represent another area of research for PW-class laser facilities (see Refs. 65–68 and references therein). When the electron energies and the laser field amplitude approach the GeV level and  $a_0 \gg 1$ , respectively, a significant portion of the electron energy is radiated away in the form of high energy photons, which in turn can decay into electron–positron pairs. This completely changes the dynamics of the laser–plasma interaction, potentially affecting laser-driven ion acceleration and high harmonics generation and providing novel sources of particles and radiation (see, e.g., Refs. 69–79 for ion acceleration). Typical setups for SFQED experiments at laser facilities, as detailed in Refs. 65–67, are either an electron beam colliding with a counter-propagating laser pulse, two colliding laser pulses, or a laser(s) interacting with a fixed plasma target. All the SFQED experiments conducted to date, starting from the SLAC E144,<sup>80,81</sup> recent GEMINI ones,<sup>82,83</sup> and planned LUXE at DESY<sup>84,85</sup> and SLAC E-320 ones, used or are going to use the first typical setup. However, with many high intensity laser facilities coming into operation in the near future<sup>86</sup> and the demonstration of the  $10^{23} \text{ W/cm}^2$  peak intensity,<sup>87</sup> other experimental setups, i.e., two colliding laser pulses and a laser(s) interacting with a fixed plasma target, start to be seriously considered for future experiments. iP2 is uniquely positioned to study the onset of SFQED effects in the intense laser interaction with fixed plasma targets. We note that the single beam geometry of iP2 presents a unique challenge for designing SFQED experiments in the interaction chamber, since the high intensity laser pulse not only needs to accelerate high energy particles and photons but also be collided with them. In its current geometry and design, iP2 can be a platform for proof-of-principle experiments on the production of gamma-ray flashes at 1 PW level in laser–solid interactions until the next 10 and 100 PW laser facilities come online. This interaction at 10 PW level can in theory produce electron–positron pairs and ultra-intense gamma-ray bursts with a high efficiency of up to 30%. For a 1 PW laser, this conversion efficiency is about 3%.<sup>88,89</sup> Experiments can be conducted at iP2 to optimize target design in order to increase the efficiency of gamma-ray



flash generation. Additionally, relativistically transparent magnetic filaments of megatesla strength can be generated during the interaction of intense laser pulses with NCD targets<sup>90,91</sup> (similar conditions as for MVA experiments). Collimated multi-MeV photons can be generated as electrons bend near the edges of this magnetic filament via synchrotron emission. These can be investigated alongside ion acceleration to study the onset of SFQED effects.

Laser-accelerated protons can be used in proton radiography to image electromagnetic fields present in dense plasmas with high temporal and spatial resolution due to their short bunch duration, high laminarity, and small source size.<sup>92</sup> The electromagnetic field distribution accompanying, for example, the growth of plasma instabilities at the back of the irradiated target can be investigated. This is of interest for fusion energy research as such instabilities severely impact the implosion symmetry. Protons generated in the same laser–target interaction are deflected in the resulting filamented electromagnetic fields and can subsequently be analyzed to investigate the instability at play<sup>93,94</sup> and shed light on the dynamics of hot electron currents. Further, multi-modal imaging becomes possible by additionally harnessing other secondary radiations that originate in the relativistic plasma.<sup>95</sup>

Ion beams are widely used for semiconductor manufacturing and more recently in the exploration of qubits and quantum materials.<sup>96</sup> Intense, short ion pulses extend the parameter space available for material processing and enable the formation of novel material phases under conditions of transient high temperature and pressure followed by rapid quenching.<sup>97</sup> Recently, the direct formation of nitrogen-vacancy centers has been reported along the tracks of swift heavy ions (such as 4 MeV/nucleon gold ions) in diamonds.<sup>98</sup> Formation of novel color center qubits, qubit assemblies, and (quantum) material phases can be explored with intense ion beams generated at iP2, where multi-species pulses of protons and heavy ions can be designed to heat, excite, dope, and transform materials.

Laser-accelerated protons using the BELLA PW laser have already been successfully used to conduct radiobiological studies at an ultra-high dose rate.<sup>12</sup> A compact proton beamline was previously implemented, which transported a few MeV proton beams, accelerated with the f/65 OAP beamline, to an irradiation site where single-layer cell samples of 1 cm diameter were irradiated with 1 Gy per shot at moderate to high repetition rates. The irradiation of normal and tumor cell samples confirmed that laser-driven protons are suitable to study radiobiological effects that are activated at ultra-high instantaneous dose rates. The new iP2 setup will deliver sufficiently higher energies to conduct volumetric irradiation of cell samples and small animals. A magnetic transport beamline has been designed to enable homogeneous irradiation of several mm diameter sample volumes<sup>99</sup> at ultra-high instantaneous dose rates.

The above-mentioned applications can be explored at iP2 and the findings will be impactful for HEDS, studies of matter under extreme conditions, fusion energy research, and radiobiology studies.

#### IV. SIMULATIONS OF THE MAGNETIC VORTEX ACCELERATION REGIME

The iP2 capabilities for advanced ion acceleration studies are showcased here with 3D particle-in-cell (PIC) simulations of the MVA regime. Simulations were performed with WarpX,<sup>100</sup> an electromagnetic, GPU-accelerated, open-source PIC code.

In the MVA regime,<sup>101,102</sup> an ultra-intense laser pulse is focused onto a NCD target and expels electrons by the ponderomotive force, creating a channel in both the electron and ion densities. Some electrons are accelerated by the non-linear wake behind the laser pulse and create an electron filament on the laser axis. An ion filament is also created due to the field structure inside the channel. The current associated with the electron filament gives rise to a magnetic field inside the self-generated channel,<sup>103</sup> which acts as a waveguide<sup>104</sup> and contains the magnetic field. When the laser pulse and the magnetic field behind it leave the target from its rear side, the magnetic field expands into the vacuum and forms a toroidal vortex in 3D. The magnetic pressure displaces the electron component of the plasma relative to the ions, and a quasistatic electric field is formed as a result of this charge separation. This field accelerates and collimates the ions from the filament.

The effectiveness of the MVA mechanism is related to the laser depositing nearly all of its energy to the fast electrons. Optimization conditions for MVA require matching the laser focal spot size to the diameter of the self-generated channel as well as matching the target thickness and density to the laser depletion length.<sup>35,101</sup> The radius of the channel is approximately given by  $R_{\text{ch}} = (\lambda/\pi)(2P/KP_c)^{1/6}(n_{\text{cr}}/n_e)^{1/3}$  in terms of the laser power  $P$ , the electron density in units of critical densities  $n_e/n_{\text{cr}}$ , the 3D geometrical factor  $K = 2/27$ , the critical power for self-focusing  $P_c = 2m_e^2 c^5 / e^2 = 17 \text{ GW}$ , and the laser wavelength  $\lambda$ . A smaller spot size compared to the channel diameter will cause filamentation due to instabilities, and a larger spot size will result in reduced efficiency of the process as intensity is decreased and some laser energy is lost to the background plasma.<sup>35</sup> The optimized length of the channel is approximately given by the laser depletion length inside the channel,  $L_{\text{ch}} = a_{\text{ch}}(n_{\text{cr}}/n_e)L_p K$ , where  $L_p$  is the length of the laser pulse and  $a_{\text{ch}}$  is the dimensionless vector potential of the laser pulse undergoing self-focusing inside the channel. In principle, the target parameters can be chosen to maximize the energy of the accelerated ions for a set of laser parameters. In our case, the laser focal spot size is fixed by the focusing optic to an anticipated FWHM of  $2.5 \mu\text{m}$ ; therefore, we match the channel diameter to this spot size by adjusting the plasma density. A series of 2D simulations, not discussed in this paper, were performed to optimize the target parameters for MVA using the iP2 beamline. For the 0.5 PW (iP2 with DPM setup) pulse focused to a  $2.5 \mu\text{m}$  focal spot, a density of  $n_e = 2n_{\text{cr}}$  and a thickness of  $L_{\text{ch}} = 28 \mu\text{m}$  were found to be the optimized conditions. NCD targets for MVA experiments may be realized in the form of supersonic gas jets,<sup>105,106</sup> thin liquid sheets,<sup>107</sup> or carbon–hydrogen (CH) foams and aerogels.<sup>108,109</sup>

#### A. Methods and algorithms

A series of 3D simulations were performed to study the robustness of the MVA mechanism as close to the experimental conditions as possible. Two parameters are of specific interest: first, it is explored if promising proton energies can be achieved even with a non-ideal laser contrast, leading to pre-expanded target profiles for the main laser pulse interaction. Second, the acceleration performance of normal and off-normal laser incidence angles are compared to model experimental constraints, where back reflections directly into the laser chain need to be avoided in the interest of laser equipment safety.

The dimensions of the simulation box are  $-20$  to  $20 \mu\text{m}$  in both transverse directions ( $x$  and  $y$ ) and  $-40$  to  $75 \mu\text{m}$  in the longitudinal direction ( $z$ ) with 1664, 1664, and 4864 cells in  $x$ ,  $y$ , and  $z$  respectively,



providing a resolution of  $\lambda_p/24$  in all three axes. Simulations were performed with the realistically anticipated laser parameters at iP2, assuming 75% and 50% energy confinement in time and space respectively, as shown in Table I. The laser is linearly polarized in x (p-polarized) with the virtual antenna positioned at  $-39\ \mu\text{m}$ ,  $1\ \mu\text{m}$  from the left boundary of the simulation window. The laser pulse has both a transverse and longitudinal Gaussian profile and propagates along the z-axis. The laser wavelength is 815 nm, and the pulse duration is 35 fs. The laser pulse is tightly focused  $2\ \mu\text{m}$  behind the target front surface at  $z = -12\ \mu\text{m}$  to a FWHM of  $2.5\ \mu\text{m}$ .

The laser intensity is  $6.05 \times 10^{21}\text{ W/cm}^2$  corresponding to an  $a_0 = 55$  without contrast cleaning and  $3.63 \times 10^{21}\text{ W/cm}^2$  corresponding to an  $a_0 = 42$  with contrast cleaning using the DPM setup. The optimized target conditions of  $n_e = 2n_{cr}$  and  $L_{ch} = 28\ \mu\text{m}$  are used for all the 3D simulations. Simulations were performed with two types of targets: pre-ionized pure hydrogen and Liquid Crystal Target 8CB (4-octyl-4'-cyanobiphenyl)  $\text{C}_{21}\text{H}_{25}\text{N}$  (LCT). Since in this setup nitrogen and carbon ions have a very similar charge-to-mass ratio, the target is simplified to  $\text{C}_{22}\text{H}_{25}$ . In order to achieve the density of  $n_e = 2n_{cr}$  for LCT, one could consider pre-expanding the target with an induced laser prepulse. Other multi-species targets that provide a similar density and mixing ratio can be considered as well.

In these PIC simulations, we used the Yee field solver with the ratio to the Courant–Friedrichs–Lewy condition set to 0.999, the Boris particle pusher, cubic (third-order) particle splines, and bilinear current filtering. Open (Silver-Mueller) simulation boundaries were applied, and the simulation box was chosen large enough that no boundary effect had an influence on the energetic, forward accelerated ions. The plasma profiles were initialized with four macroparticles of each ion species and the same number of scaled electron macroparticles per cell (16 macroparticles per cell in total). The initial electron temperature was assumed to be Maxwellian, with a Gaussian distribution of width  $u_{x,y,z}^{\text{th}} = 0.01\beta\gamma$  in each component. Complete simulation input files are provided in the supplementary material.<sup>110</sup> Simulations ran up to 1 ps and generally were stopped when the maximum ion energy had converged. All algorithms in WarpX are CUDA accelerated, and 3D simulations were executed on the GPU-accelerated Summit supercomputer at OLCF.<sup>111</sup>

Simulations were performed with both  $\theta = 0^\circ$  and  $25^\circ$  angle of incidence, available for the initial experiments at iP2, to study the performance of the MVA mechanism under a normal and off-normal angle of incidence. Additionally, exponential density ramps with  $\sigma = 1\text{--}5\ \mu\text{m}$  scale lengths were added to the target symmetrically at the front and rear sides to study the effects of preplasma and target

expansion as close to the foreseen experimental conditions as possible. The exponential preplasma profile was cut off to zero  $25\ \mu\text{m}$  from the target surfaces, far in the undercritical density region, to reduce numerical costs.

The density ramp parameter range was chosen for the following reasons. Prior theoretical studies of MVA<sup>101</sup> suggest that sharp density gradients at the target rear lead to high accelerating fields and, thus, high particle energies. In the case of an experimentally realistic laser contrast, including the amplified spontaneous emission background, prepulses, and the main pulse rising edge (typically existing in the last hundreds of fs before arrival of the peak intensity), it is common that the target undergoes hydrodynamic pre-expansion.<sup>112</sup> In our simulations, we accounted for this pre-expansion by adding an exponential preplasma to the target profile as a parameter. We assumed a target profile with a symmetric pre-expansion on both the target front and rear on these time scales. We note that reduced pre-expansion at the target rear would at best improve the rear acceleration conditions further. We expect to gain control over some of these aspects with the planned DPM setup in combination with an artificial, controlled prepulse. For this capability study, the performance without the DPM and the effects of non-ideal laser contrast cleaning are of interest.

## B. Simulation results

Characterized ion beams from a subset of the performed 3D simulations are shown in Fig. 5 at  $t = 407\text{ fs}$ . The ion beam kinetic energy spectra are shown in Figs. 5(b) and 5(d) as well as the divergence of the ion beams in Figs. 5(a) and 5(c). Simulations performed with pure hydrogen targets are presented (a) and (b) as well as simulations performed with LCT (c) and (d) with carbon ions shown in the inset plots. For the case of pure hydrogen target, the cutoff kinetic energy of protons ranges from 70 to 110 MeV. For the simulations performed with LCT, the cutoff kinetic energy of protons ranges from 59 to 89 MeV, and the maximum kinetic energy per nucleon for carbon ions is in the range of 21–29 MeV. The generated ion beams have a low divergence in all cases with the divergence angle, defined as  $2\Delta\theta = 2\sqrt{\langle(\theta^2)\rangle - \langle\theta\rangle^2}$ , between  $7^\circ$  and  $15^\circ$  for  $E > 0.4E_{i,\text{max}}$ . Here,  $\langle\theta\rangle$  is the average of the angular distribution in each energy bin, and  $\theta$  is defined as the angle to the laser axis,  $\theta = \sin^{-1}(p_\perp/p)$  with  $p_\perp = \sqrt{p_x^2 + p_y^2}$  and  $p = \sqrt{p_x^2 + p_y^2 + p_z^2}$ . The energy in Figs. 5(a) and 5(c) is normalized to the maximum ion energy in the respective run and for the specific ion species,  $E_{i,\text{max}}$ . This narrow divergence results from the transverse electric field generated at the target rear side.<sup>35</sup> Reduced angular divergence has also been reported from previous experiments with NCD targets.<sup>32</sup> The number of accelerated ions per MeV per steradian is on the order of  $10^9$  near the cutoff energy consistently for all the simulations and species. At the lower energies, between 1 and 30 MeV, the number of accelerated protons per MeV per steradian is between  $10^{10}$  and  $10^{13}$ , which is an order of magnitude higher compared to results from previous experiments producing high flux proton beams.<sup>31,38,40</sup> These experiments generated maximum proton energies on the order of 10 MeV. Presented MVA simulations show comparable flux for higher energies up to 100 MeV. Similar spectra have been measured in experiments from an enhanced hybrid scheme.<sup>29</sup>

TABLE I. Representative parameters for the iP2 beamline used in simulations.

Laser parameters	Value without DPM	Value with DPM
Pulse energy (J)	40	24
Pulse length (fs)	35	35
Peak power (PW)	0.9	0.5
Central wavelength ( $\mu\text{m}$ )	0.815	0.815
Focus size in FWHM ( $\mu\text{m}$ )	2.5	2.5
Peak intensity ( $\text{W/cm}^2$ )	$6.0 \times 10^{21}$	$3.6 \times 10^{21}$
Peak $a_0$	55	42

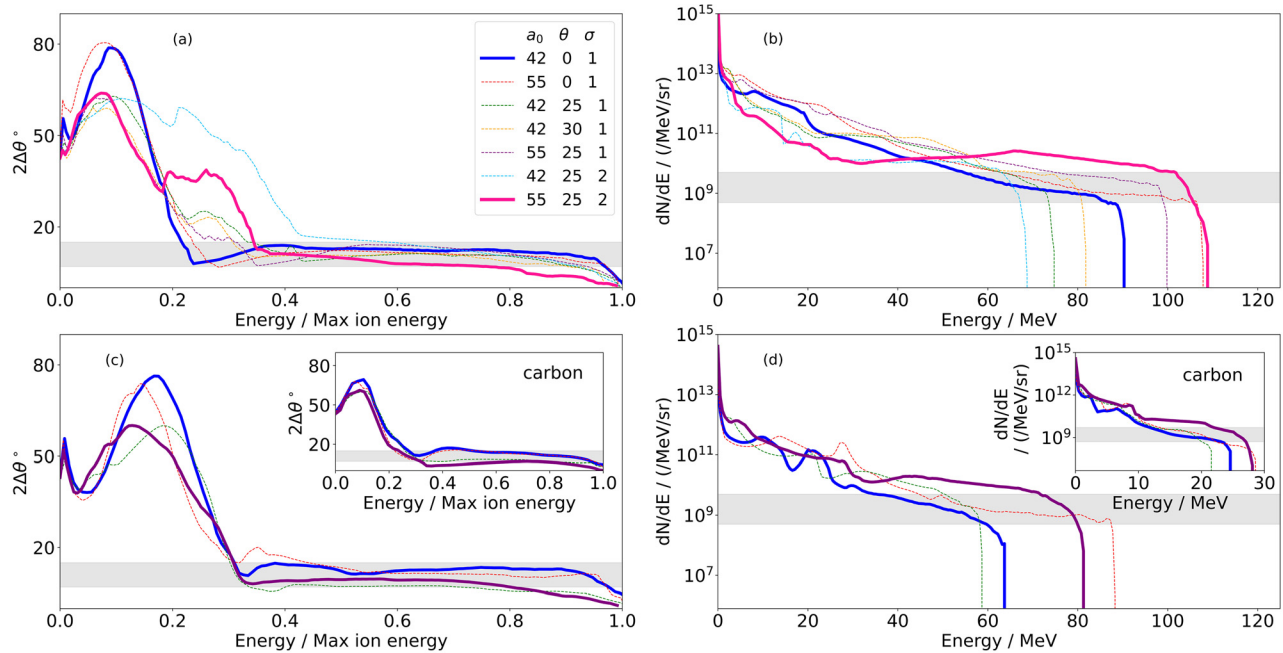


**FIG. 5.** An overview of the generated ion beams from various MVA simulations is shown. Simulations with pure hydrogen are given in (a) and (b) and simulations with LCT are given in (c) and (d) with carbon ions shown in the insets. Divergence vs normalized kinetic energy is given in (a) and (c) with the shaded-gray area marking  $7^\circ$ – $15^\circ$  range. The ion kinetic energy spectra are given in (b) and (d) with the shaded-gray area marking count between  $5 \times 10^8$  and  $5 \times 10^9$   $1/\text{MeV/sr}$ . The highlighted simulations are the case with  $a_0 = 42$ , target tilt of  $\theta = 0^\circ$ , and preplasma scale length of  $\sigma = 1 \mu\text{m}$  (solid blue), the case with the highest energy protons with  $a_0 = 55$ ,  $\theta = 25^\circ$ , and  $\sigma = 2 \mu\text{m}$  (solid magenta) and the LCT simulation with  $a_0 = 55$ ,  $\theta = 25^\circ$ , and  $\sigma = 1 \mu\text{m}$  (purple).

The maximum proton kinetic energy observed at a later time,  $t = 670$  fs, is 125 MeV for a hydrogen target simulation with  $a_0 = 55$ , target tilt of  $25^\circ$ , and preplasma scale length of  $2 \mu\text{m}$ , and 91 MeV for a composite target simulation with  $a_0 = 55$ , target tilt of  $0^\circ$ , and preplasma scale length of  $1 \mu\text{m}$ . The maximum carbon kinetic energy is 37 MeV/nucleon from a simulation with  $a_0 = 55$ , target tilt of  $25^\circ$ , and preplasma scale length of  $2 \mu\text{m}$ . These maximum proton energies are consistent with previous MVA simulations and scalings.<sup>35</sup> However, the simulations presented in this paper use laser parameters that will be available soon. The 125 MeV energy, if achieved in experiments, would be a breakthrough for laser-driven proton acceleration as proton energies beyond 100 MeV have not yet been measured. The maximum observed carbon energy is also in agreement with previous MVA simulations<sup>113</sup> and comparable with experimental results. Previous experiments with NCD plasmas<sup>38</sup> produced up to 20 MeV/nucleon carbon ions. In addition, experiments conducted in the RPA regime have reported preferential acceleration of carbon ions to a similar energy of 35 MeV/nucleon.<sup>30</sup>

Simulations performed with a preplasma scale length of  $5 \mu\text{m}$  produced maximum kinetic energies between 30 and 90 MeV for protons and between 10 and 27 MeV/nucleon for carbon ions; however, the beam profile and divergence are not comparable to results from other simulations with a smaller preplasma scale length. As MVA is sensitive to the acceleration length<sup>101</sup> as well as the homogeneity of the plasma,<sup>21,113,114</sup> it is likely that the target thickness needs to be adjusted for the tilt and the additional density ramp. Further, the location of the focal spot might need to move back in the case of a long density ramp. Ultimately, preplasma scale length may be a knob to control the

acceleration length and the quality of the ion beams generated in experiments.

The electron and ion density distributions from one of the LCT simulations ( $a_0 = 55$ ,  $\theta = 25^\circ$ ,  $\sigma = 1 \mu\text{m}$ ) at  $t = 271$  fs are shown in Figs. 6(a) and 6(b). For this simulation, this time corresponds to the laser pulse exiting the target from the rear side. In general, the electron and ion channels are robustly generated in simulations with tilted targets as is shown here for this simulation. An electron and an ion filament are formed on the laser axis inside the channels. The stream of accelerated electrons generates a strong azimuthal magnetic field on the order of 0.1 MT, shown in Figs. 6(c) and 6(d), as expected for a PW laser pulse. The azimuthal magnetic field is plotted as  $B_y$  in the  $xz$  plane to show the vortex in the tilted geometry and as  $B_x$  in the  $yz$  plane to visualize it separately from the magnetic field of the laser in the  $y$ -direction. The expansion of the magnetic field as it leaves the target displaces surface electrons and results in a strong longitudinal electric field behind the rear surface of the target. This field is on the order of tens of TV/m, shown in Figs. 6(e) and 6(f), and accelerates ions from the central ion filament inside the channel. The transverse electric field, shown in Fig. 6(g), collimates the accelerated ion beam. The ion phase space at  $t = 317$  fs is shown in Fig. 7. The laser pulse passed the target and the longitudinal electric field at three time steps, immediately before and after the laser pulse exits the target and at a time when proton energy is almost converged, are overlaid to show the evolution of the accelerating electric field.

Simulations show the generation of high energy electrons, a signature of the MVA mechanism. The maximum electron kinetic energy

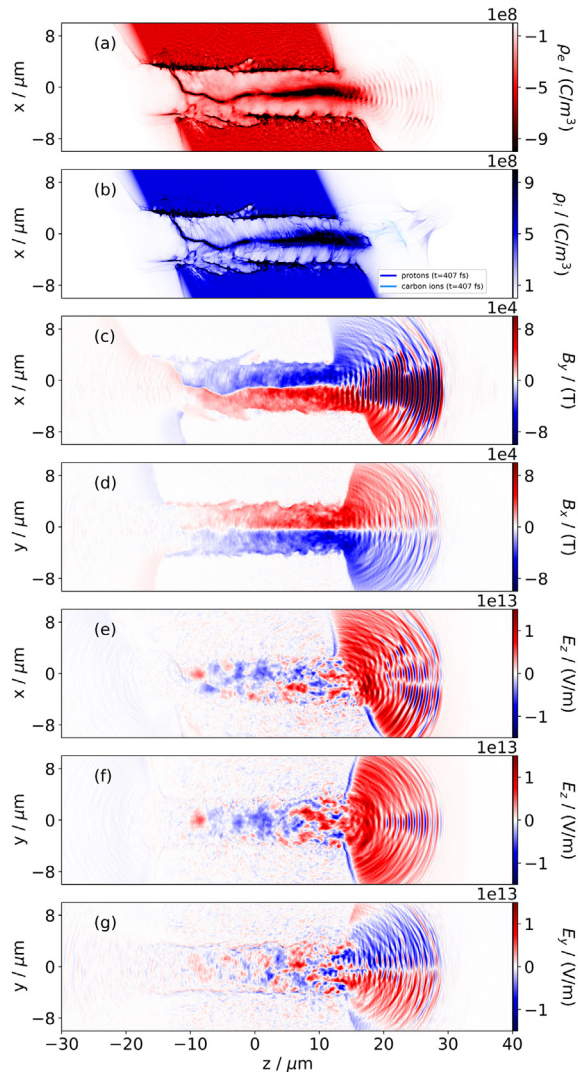


**FIG. 6.** Composite target simulation results from the case of  $a_0 = 55$ , target tilt of  $25^\circ$ , and preplasma scale length of  $1 \mu\text{m}$  are shown. (a) Electron density, (b) ion density including protons and carbon ions, (c) azimuthal magnetic field shown as  $B_y$  in the  $xz$  plane, (d) azimuthal magnetic field shown as  $B_x$  in the  $yz$  plane, (e) and (f)  $E_z$  field in the vertical and horizontal slices, and (g)  $E_y$  focusing field are shown early in the acceleration stage at  $t = 271$  fs. Accelerated protons and carbon ions at  $t = 407$  fs are also overlaid in (b) showing ion acceleration in the target normal direction.

is 540 MeV at  $t = 226$  fs, about the time that the laser pulse exits the target. The maximum proton kinetic energy at this time is  $\sim 20$  MeV. In the next  $\sim 140$  fs, the acceleration stage, proton kinetic energy increases to  $\sim 80$  MeV, a steep rise in energy during the time of magnetic field expansion. The longitudinal electric field is short lived and dissipates quickly. Proton energy continues to increase in the following  $\sim 200$  fs to 85 MeV before the simulation stops. From the initial 40 J of the laser energy, 0.64 J is transferred to the combined proton and carbon ion beams implying a 1.6% conversion efficiency. From this 0.64 J,

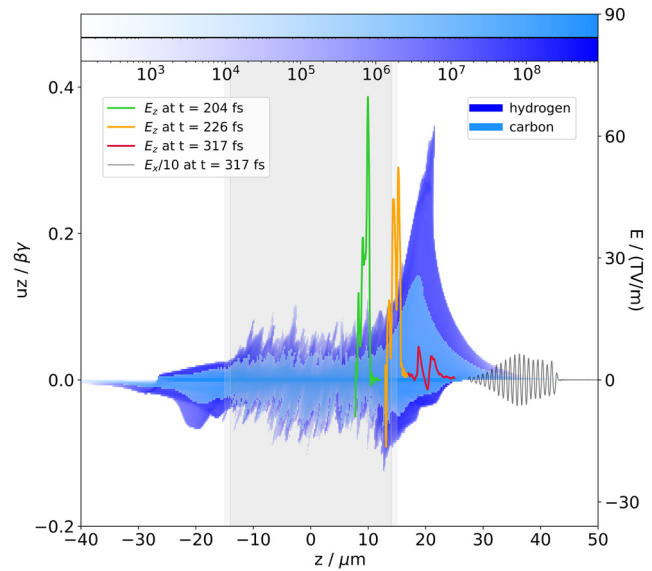


**FIG. 7.** Ion phase space, protons in dark blue and carbon ions overlaid in light blue, is shown during the acceleration stage at  $t = 317$  fs along with the laser field,  $E_x$  (black). The accelerating electric field,  $E_z$  (green, yellow, red), is shown immediately before and after the laser pulse exits the target and at a time when proton energy is almost converged. The shaded region represents the original location of the NCD target.

70.56%, 14.65%, 4.45%, and 0.27% are transferred to protons with  $E < 25$ ,  $25 < E < 50$ ,  $50 < E < 75$ , and  $75 < E$  MeV, respectively, and the remaining 10.07% is transferred to carbon ions. The ions from the tilted target geometry are accelerated in the normal direction to the rear side of the target as shown in the ion density plot, Fig. 6(b), where accelerated protons and carbon ions at  $t = 407$  fs are plotted. The final angularly resolved energy spectra, Fig. 8, confirm this by showing the accelerated ions at  $\sim 25^\circ$  angle with respect to the laser axis. The insets are the integrated spatial distribution of accelerated protons with energy between 40 and 60 MeV, and carbon ions with energy between 20 and 40 MeV/nucleon, showing the center of the beams offset from the laser axis in the  $x$ -direction.

## V. CONCLUSIONS

A new platform to study laser–solid interactions at the BELLA Center using the 1 Hz BELLA PW beamline, named iP2, has been constructed and will be used to conduct experiments in the near future. The beamline is well suited to investigate advanced ion acceleration mechanisms requiring ultra-high intensities, substantial control over the temporal contrast, and high repetition rates to explore a multi-dimensional parameter space to optimize a certain acceleration regime and investigate transitions between them. For example, the DPM-cleaned contrast will allow for ion acceleration from nm thick and structured targets as it is important that the shape of the target is not altered by prepulses prior to the arrival of the main pulse. Additionally, operating experiments at high repetition rates will allow for the implementation of feedback loops to control ion beam parameters and increase their stability. An increased stability of the accelerator will be beneficial in mapping ion beam characteristics to the evolving



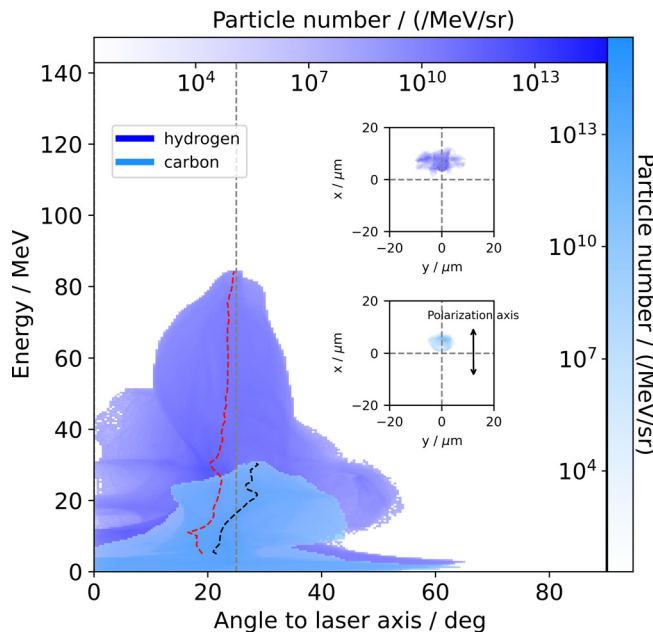


**FIG. 8.** The final angularly resolved energy spectra, from the tilted target simulation, are shown for both hydrogen and carbon ions at  $t = 543$  fs. Selected ions are forward accelerated for positions  $z > 25 \mu\text{m}$ . The vertical, gray dashed line marks the  $25^\circ$  angle, normal to the target rear surface. The other dashed lines show the average angle per energy bin for hydrogen (red) and for carbon (black). The insets are the integrated spatial distribution of accelerated protons with energy between 40 and 60 MeV and carbon ions with energy between 20 and 40 MeV/nucleon in the  $xy$  plane. The centers of the beams are offset from the laser axis in the  $x$ -direction toward the target normal direction.

laser and plasma parameters.<sup>115</sup> It should be noted that besides optimized laser parameters, the design and fabrication of suitable targets are essential to reach advanced acceleration regimes. Scaling laws for advanced mechanisms, such as RPA and MVA, may be verified experimentally in the near future at iP2, and the results will be beneficial for the design and development of future laser-driven accelerators for research as well as various applications in medicine, energy, and industry.

In preparation for the upcoming first experimental campaign at iP2, 3D PIC simulations were performed with iP2 parameters and demonstrated acceleration of ion beams in the MVA regime with a robust performance against target tilt and preplasma scale length. Proton beams with energy up to 125 MeV, divergence of  $\sim 10^\circ$ , and flux of  $10^8$ – $10^9$ /MeV/sr were demonstrated with  $\sim 1\%$  conversion efficiency of the laser pulse to proton beam energy.

## ACKNOWLEDGMENTS

This work was supported by the U.S. Department of Energy (DOE) Office of Science, Offices of Fusion Energy Sciences (FES) and High Energy Physics, LaserNetUS, and used resources at NERSC under Contract No. DE-AC02-05CH11231 as well as OLCF (No. DE-AC05-00OR22725). S. Hakimi was supported by the U.S. DOE FES Postdoctoral Research Program administered by the Oak Ridge Institute for Science and Education (ORISE) for the DOE. ORISE is managed by Oak Ridge Associated Universities

(ORAU) under Contract No. DE-SC0014664. All opinions expressed in this paper are those of the authors and do not necessarily reflect the policies and views of DOE, ORAU, or ORISE. WarpX was supported by the Exascale Computing Project (No. 17-SC-20-SC), a collaborative effort of two U.S. DOE organizations (Office of Science and the National Nuclear Security Administration).

We gratefully acknowledge technical support from Zachary Eisentraut, Mark Kirkpatrick, Tyler Sipla, Jonathan Bradford, Haris Muratagic, Gregory Scharfstein, Nathan Ybarrolaza, Gregg Mannino, Paul Centeno, Thorsten Stezelberger, Arturo Magana, Joe Riley, the Radiation Protection Group, and the EH&S Division of LBNL. The contributions of W. P. Leemans, who initially led this project, were made prior to his departure from LBNL to DESY in 2019. We would also like to thank Remi Lehe, Carlo Benedetti, Marlene Turner, Jian Hui Bin, Qing Ji, Josh Stackhouse, Jared De Chant, and Alexander Picksley for useful discussions. We thank all the contributors from the WarpX community who participated in code improvement.

## AUTHOR DECLARATIONS

### Conflict of Interest

The authors have no conflicts to disclose.

## Author Contributions

**Sahel Hakimi:** Conceptualization (equal); Data curation (equal); Formal analysis (lead); Funding acquisition (supporting); Investigation (lead); Methodology (equal); Software (supporting); Validation (equal); Visualization (lead); Writing—original draft (lead); Writing—review and editing (lead). **Lieselotte Obst-Huebl:** Conceptualization (equal); Data curation (supporting); Formal analysis (supporting); Investigation (supporting); Methodology (equal); Validation (equal); Visualization (supporting); Writing—original draft (supporting); Writing—review and editing (supporting). **Axel Huebl:** Conceptualization (equal); Data curation (equal); Formal analysis (supporting); Funding acquisition (equal); Investigation (supporting); Methodology (equal); Resources (lead); Software (lead); Validation (equal); Visualization (supporting); Writing—original draft (supporting); Writing—review and editing (supporting). **Kei Nakamura:** Conceptualization (equal); Data curation (supporting); Formal analysis (supporting); Investigation (supporting); Methodology (equal); Project administration (supporting); Supervision (supporting); Validation (equal); Visualization (supporting); Writing—original draft (supporting); Writing—review and editing (supporting). **Stepan S. Bulanov:** Conceptualization (equal); Data curation (supporting); Formal analysis (supporting); Investigation (supporting); Methodology (equal); Supervision (supporting); Validation (equal); Visualization (supporting); Writing—original draft (supporting); Writing—review and editing (supporting). **Sven Steinke:** Conceptualization (equal); Funding acquisition (equal); Writing—review and editing (supporting). **Wim P. Leemans:** Conceptualization (equal); Funding acquisition (equal); Writing—review and editing (supporting). **Zachary Kober:** Formal analysis (supporting); Visualization (supporting). **Tobias M. Ostermayr:** Conceptualization (equal); Writing—review and editing (supporting). **Thomas Schenkel:** Conceptualization (equal); Funding



acquisition (supporting); Project administration (supporting); Writing—original draft (supporting); Writing—review and editing (supporting). **Anthony J Gonsalves:** Conceptualization (equal); Project administration (supporting); Supervision (supporting); Visualization (supporting); Writing—review and editing (supporting). **Jean-Luc Vay:** Conceptualization (equal); Funding acquisition (supporting); Resources (lead); Software (lead); Supervision (lead); Writing—review and editing (supporting). **Jeroen van Tilborg:** Conceptualization (equal); Project administration (supporting); Supervision (supporting); Writing—review and editing (supporting). **Csaba Toth:** Conceptualization (equal); Project administration (supporting); Validation (supporting); Writing—review and editing (supporting). **Carl B. Schroeder:** Conceptualization (equal); Supervision (supporting); Writing—review and editing (supporting). **Eric Esarey:** Conceptualization (equal); Funding acquisition (equal); Project administration (lead); Supervision (lead); Writing—review and editing (supporting). **Cameron G.R. Geddes:** Conceptualization (equal); Funding acquisition (equal); Project administration (supporting); Supervision (lead); Writing—review and editing (supporting). L. Obst-Huebl and K. Nakamura led the final design and implementation of the IP2 beamline, and S. Steinke the initial design.

## DATA AVAILABILITY

The data that support the findings of this study are openly available in Zenodo at <https://zenodo.org/record/6050002>, Ref. 110.

## REFERENCES

- E. Esarey, C. Schroeder, and W. P. Leemans, "Physics of laser-driven plasma-based electron accelerators," *Rev. Mod. Phys.* **81**, 1229 (2009).
- H. Daido, M. Nishiuchi, and A. S. Pirozhkov, "Review of laser-driven ion sources and their applications," *Rep. Prog. Phys.* **75**, 056401 (2012).
- A. Macchi, M. Borghesi, and M. Passoni, "Ion acceleration by superintense laser-plasma interaction," *Rev. Mod. Phys.* **85**, 751 (2013).
- S. M. Hooker, "Developments in laser-driven plasma accelerators," *Nat. Photonics* **7**, 775–782 (2013).
- S. S. Bulanov, Q. Ji, S. Steinke, T. Schenkel, E. Esarey, and W. P. Leemans, "Advanced acceleration mechanisms for laser driven ions by PW-lasers," in *7th International Particle Accelerator Conference (IPAC'16)*, Busan, Korea, May 8–13, 2016, <http://www.jacow.org>, pp. 2082–2084.
- T. Cowan, J. Fuchs, H. Ruhl, A. Kemp, P. Audebert, M. Roth, R. Stephens, I. Barton, A. Blazevic, E. Brambrink *et al.*, "Ultralow emittance, multi-MeV proton beams from a laser virtual-cathode plasma accelerator," *Phys. Rev. Lett.* **92**, 204801 (2004).
- S. V. Bulanov, J. J. Wilkens, T. Z. Esirkepov, G. Korn, G. Kraft, S. D. Kraft, M. Molls, and V. S. Khoroskov, "Laser ion acceleration for hadron therapy," *Phys.-Usp.* **57**, 1149 (2014).
- M. Roth, T. Cowan, M. Key, S. Hatchett, C. Brown, W. Fountain, J. Johnson, D. Pennington, R. Snavely, S. Wilks *et al.*, "Fast ignition by intense laser-accelerated proton beams," *Phys. Rev. Lett.* **86**, 436 (2001).
- M. Borghesi, J. Fuchs, S. Bulanov, A. Mackinnon, P. Patel, and M. Roth, "Fast ion generation by high-intensity laser irradiation of solid targets and applications," *Fusion Sci. Technol.* **49**, 412–439 (2006).
- P. Patel, A. Mackinnon, M. Key, T. Cowan, M. Foord, M. Allen, D. Price, H. Ruhl, P. Springer, and R. Stephens, "Isochoric heating of solid-density matter with an ultrafast proton beam," *Phys. Rev. Lett.* **91**, 125004 (2003).
- A. A. Friedl, K. M. Prise, K. T. Butterworth, P. Montay-Gruel, and V. Favaudon, "Radiobiology of the flash effect," *Med. Phys.* **49**, 1993 (2021).
- J. Bin, L. Obst-Huebl, J.-H. Mao, K. Nakamura, L. D. Geulig, H. Chang, Q. Ji, L. He, J. De Chant, Z. Kober *et al.*, "A new platform for ultra-high dose rate radiobiological research using the BELLA PW laser proton beamline," *Sci. Rep.* **12**, 1484 (2022).
- U. Masood, M. Bussmann, T. Cowan, W. Enghardt, L. Karsch, F. Kroll, U. Schramm, and J. Pawelke, "A compact solution for ion beam therapy with laser accelerated protons," *Appl. Phys. B* **117**, 41–52 (2014).
- S. Wilks, A. Langdon, T. Cowan, M. Roth, M. Singh, S. Hatchett, M. Key, D. Pennington, A. MacKinnon, and R. Snavely, "Energetic proton generation in ultra-intense laser–solid interactions," *Phys. Plasmas* **8**, 542–549 (2001).
- I. Last, I. Schek, and J. Jortner, "Energetics and dynamics of coulomb explosion of highly charged clusters," *J. Chem. Phys.* **107**, 6685–6692 (1997).
- T. Ditmire, J. Tisch, E. Springate, M. Mason, N. Hay, R. Smith, J. Marangos, and M. Hutchinson, "High-energy ions produced in explosions of superheated atomic clusters," *Nature* **386**, 54–56 (1997).
- T. Esirkepov, M. Borghesi, S. V. Bulanov, G. Mourou, and T. Tajima, "Highly efficient relativistic-ion generation in the laser-piston regime," *Phys. Rev. Lett.* **92**, 175003 (2004).
- L. O. Silva, M. Marti, J. R. Davies, R. A. Fonseca, C. Ren, F. S. Tsung, and W. B. Mori, "Proton shock acceleration in laser-plasma interactions," *Phys. Rev. Lett.* **92**, 015002 (2004).
- D. Haberberger, S. Tochitsky, F. Fiuza, C. Gong, R. A. Fonseca, L. O. Silva, W. B. Mori, and C. Joshi, "Collisionless shocks in laser-produced plasma generate monoenergetic high-energy proton beams," *Nat. Phys.* **8**, 95–99 (2012).
- A. V. Kuznetsov, T. Z. Esirkepov, F. F. Kamenets, and S. V. Bulanov, "Efficiency of ion acceleration by a relativistically strong laser pulse in an underdense plasma," *Plasma Phys. Rep.* **27**, 211–220 (2001).
- S. V. Bulanov, D. V. Dylov, T. Z. Esirkepov, F. F. Kamenets, and D. V. Sokolov, "Ion acceleration in a dipole vortex in a laser plasma corona," *Plasma Phys. Rep.* **31**, 369–381 (2005).
- S. V. Bulanov and T. Z. Esirkepov, "Comment on 'Collimated multi-MeV ion beams from high-intensity laser interactions with underdense plasma,'" *Phys. Rev. Lett.* **98**, 049503 (2007).
- F. Wagner, C. Brabetz, O. Deppert, M. Roth, T. Stöhlker, A. Tauschwitz, A. Tebartz, B. Zielbauer, and V. Bagnoud, "Accelerating ions with high-energy short laser pulses from submicrometer thick targets," *High Power Laser Sci. Eng.* **4**, E45 (2016).
- F. Wagner, O. Deppert, C. Brabetz, P. Fiala, A. Kleinschmidt, P. Poth, V. Schanz, A. Tebartz, B. Zielbauer, M. Roth *et al.*, "Maximum proton energy above 85 MeV from the relativistic interaction of laser pulses with micrometer thick CH<sub>2</sub> targets," *Phys. Rev. Lett.* **116**, 205002 (2016).
- A. Henig, S. Steinke, M. Schnürer, T. Sokollik, R. Hörlein, D. Kiefer, D. Jung, J. Schreiber, B. Hegelich, X. Yan *et al.*, "Radiation-pressure acceleration of ion beams driven by circularly polarized laser pulses," *Phys. Rev. Lett.* **103**, 245003 (2009).
- S. Kar, K. Kakolee, B. Qiao, A. Macchi, M. Cerchez, D. Doria, M. Geissler, P. McKenna, D. Neely, J. Osterholz *et al.*, "Ion acceleration in multispecies targets driven by intense laser radiation pressure," *Phys. Rev. Lett.* **109**, 185006 (2012).
- S. Steinke, P. Hilz, M. Schnürer, G. Priebe, J. Bränzel, F. Abicht, D. Kiefer, C. Kreuzer, T. Ostermayr, J. Schreiber *et al.*, "Stable laser-ion acceleration in the light sail regime," *Phys. Rev. Spec. Top.-Accel. Beams* **16**, 011303 (2013).
- I. J. Kim, K. H. Pae, I. W. Choi, C.-L. Lee, H. T. Kim, H. Singhal, J. H. Sung, S. K. Lee, H. W. Lee, P. V. Nickles *et al.*, "Radiation pressure acceleration of protons to 93 MeV with circularly polarized petawatt laser pulses," *Phys. Plasmas* **23**, 070701 (2016).
- A. Higginson, R. Gray, M. King, R. Dance, S. Williamson, N. Butler, R. Wilson, R. Capdessus, C. Armstrong, J. Green *et al.*, "Near-100 MeV protons via a laser-driven transparency-enhanced hybrid acceleration scheme," *Nat. Commun.* **9**, 724 (2018).
- A. McIlvenny, D. Doria, L. Romagnani, H. Ahmed, N. Booth, E.-J. Ditter, O. Ettlinger, G. Hicks, P. Martin, G. G. Scott *et al.*, "Selective ion acceleration by intense radiation pressure," *Phys. Rev. Lett.* **127**, 194801 (2021).
- A. Yogo, H. Daido, S. Bulanov, K. Nemoto, Y. Oishi, T. Nayuki, T. Fujii, K. Ogura, S. Orimo, A. Sagisaka *et al.*, "Laser ion acceleration via control of the near-critical density target," *Phys. Rev. E* **77**, 016401 (2008).
- L. Willingale, S. Nagel, A. G. R. Thomas, C. Bellei, R. J. Clarke, A. E. Dangor, R. Heathcote, M. C. Kaluza, C. Kamperidis, S. Kneip *et al.*, "Characterization of high-intensity laser propagation in the relativistic transparent regime through measurements of energetic proton beams," *Phys. Rev. Lett.* **102**, 125002 (2009).

- <sup>33</sup>L. Willingale, P. Nilson, A. G. R. Thomas, S. S. Bulanov, A. Maksimchuk, W. Nazarov, T. Sangster, C. Stoeckl, and K. Krushelnick, "High-power, kilojoule laser interactions with near-critical density plasma," *Phys. Plasmas* **18**, 056706 (2011).
- <sup>34</sup>S. S. Bulanov, E. Esarey, C. B. Schroeder, S. V. Bulanov, T. Z. Esirkepov, M. Kando, F. Pegoraro, and W. P. Leemans, "Radiation pressure acceleration: The factors limiting maximum attainable ion energy," *Phys. Plasmas* **23**, 056703 (2016).
- <sup>35</sup>J. Park, S. S. Bulanov, J. Bin, Q. Ji, S. Steinke, J.-L. Vay, C. G. Geddes, C. B. Schroeder, W. P. Leemans, T. Schenkel *et al.*, "Ion acceleration in laser generated megatesla magnetic vortex," *Phys. Plasmas* **26**, 103108 (2019).
- <sup>36</sup>F. Dollar, S. Reed, J. Matsuoka, S. Bulanov, V. Chvykov, G. Kalintchenko, C. McGuffey, P. Rousseau, A. Thomas, L. Willingale *et al.*, "High-intensity laser-driven proton acceleration enhancement from hydrogen containing ultrathin targets," *Appl. Phys. Lett.* **103**, 141117 (2013).
- <sup>37</sup>L. Willingale, S. Mangles, P. Nilson, R. Clarke, A. Dangor, M. Kaluza, S. Karsch, K. Lancaster, W. Mori, Z. Najmudin *et al.*, "Collimated multi-MeV ion beams from high-intensity laser interactions with underdense plasma," *Phys. Rev. Lett.* **96**, 245002 (2006).
- <sup>38</sup>J. Bin, W. Ma, H. Wang, M. Streeter, C. Kreuzer, D. Kiefer, M. Yeung, S. Couzens, P. Foster, B. Dromey *et al.*, "Ion acceleration using relativistic pulse shaping in near-critical-density plasmas," *Phys. Rev. Lett.* **115**, 064801 (2015).
- <sup>39</sup>M. Helle, D. Gordon, D. Kaganovich, Y. Chen, J. Palastro, and A. Ting, "Laser-accelerated ions from a shock-compressed gas foil," *Phys. Rev. Lett.* **117**, 165001 (2016).
- <sup>40</sup>S. Steinke, J. Bin, J. Park, Q. Ji, K. Nakamura, A. Gonsalves, S. S. Bulanov, M. Thévenet, C. Toth, J.-L. Vay *et al.*, "Acceleration of high charge ion beams with achromatic divergence by petawatt laser pulses," *Phys. Rev. Accel. Beams* **23**, 021302 (2020).
- <sup>41</sup>D. Batani, R. Jafer, M. Veltcheva, R. Dezulian, O. Lundh, F. Lindau, A. Persson, K. Osvey, C. Wahlström, D. Carroll *et al.*, "Effects of laser prepulses on laser-induced proton generation," *New J. Phys.* **12**, 045018 (2010).
- <sup>42</sup>T. Z. Esirkepov, J. K. Koga, A. Sunahara, T. Morita, M. Nishikino, K. Kageyama, H. Nagatomo, K. Nishihara, A. Sagisaka, H. Kotaki *et al.*, "Prepulse and amplified spontaneous emission effects on the interaction of a petawatt class laser with thin solid targets," *Nucl. Instrum. Methods Phys. Res., Sect. A* **745**, 150–163 (2014).
- <sup>43</sup>E. McLean, S. Gold, J. Stamper, R. Whitlock, H. Griem, S. Obenschain, B. Ripin, S. Bodner, M. Herbst, S. Gitomer *et al.*, "Preheat studies for foils accelerated by ablation due to laser irradiation," *Phys. Rev. Lett.* **45**, 1246 (1980).
- <sup>44</sup>K. Nakamura, H.-S. Mao, A. J. Gonsalves, H. Vincenti, D. E. Mittelberger, J. Daniels, A. Magana, C. Toth, and W. P. Leemans, "Diagnostics, control and performance parameters for the BELLA high repetition rate petawatt class laser," *IEEE J. Quantum Electron.* **53**, 1–21 (2017).
- <sup>45</sup>H.-E. Tsai, C. Geddes, T. Ostermayr, G. Muñoz, J. van Tilborg, S. Barber, F. Isono, H.-S. Mao, K. Swanson, R. Lehe *et al.*, "Laser-plasma-accelerator-driven quasi-monoenergetic MeV Thomson photon source and laser facility," in *2018 IEEE Advanced Accelerator Concepts Workshop (AAC)* (IEEE, 2018) pp. 1–5.
- <sup>46</sup>F. Isono, J. van Tilborg, S. K. Barber, J. Natal, C. Berger, H.-E. Tsai, T. Ostermayr, A. Gonsalves, C. Geddes, and E. Esarey, "High-power non-perturbative laser delivery diagnostics at the final focus of 100-TW-class laser pulses," *High Power Laser Sci. Eng.* **9**, E25 (2021).
- <sup>47</sup>W. P. Leemans, A. Gonsalves, H.-S. Mao, K. Nakamura, C. Benedetti, C. Schroeder, C. Tóth, J. Daniels, D. Mittelberger, S. S. Bulanov *et al.*, "Multi-GeV electron beams from capillary-discharge-guided subpetawatt laser pulses in the self-trapping regime," *Phys. Rev. Lett.* **113**, 245002 (2014).
- <sup>48</sup>A. Gonsalves, K. Nakamura, J. Daniels, C. Benedetti, C. Pieronek, T. De Raadt, S. Steinke, J. Bin, S. Bulanov, J. Van Tilborg *et al.*, "Petawatt laser guiding and electron beam acceleration to 8 GeV in a laser-heated capillary discharge waveguide," *Phys. Rev. Lett.* **122**, 084801 (2019).
- <sup>49</sup>LaserNetUS: High Intensity Laser Research, [lasernetus.org](http://lasernetus.org).
- <sup>50</sup>A. Zingale, N. Czapla, D. Nasir, S. Barber, J. Bin, A. Gonsalves, F. Isono, J. van Tilborg, S. Steinke, K. Nakamura *et al.*, "Emittance preserving thin film plasma mirrors for GeV scale laser plasma accelerators," *Phys. Rev. Accel. Beams* **24**, 121301 (2021).
- <sup>51</sup>A. Jeandet, A. Borot, K. Nakamura, S. W. Jolly, A. J. Gonsalves, C. Tóth, H.-S. Mao, W. P. Leemans, and F. Quéré, "Spatio-temporal structure of a petawatt femtosecond laser beam," *J. Phys.* **1**, 035001 (2019).
- <sup>52</sup>A. Jeandet, S. W. Jolly, A. Borot, B. Bussière, P. Dumont, J. Gautier, O. Gobert, J.-P. Goddet, A. Gonsalves, A. Irman *et al.*, "Survey of spatio-temporal couplings throughout high-power ultrashort lasers," *Opt. Express* **30**, 3262–3288 (2022).
- <sup>53</sup>S. Steinke, J. Van Tilborg, C. Benedetti, C. Geddes, J. Daniels, K. Swanson, A. Gonsalves, K. Nakamura, B. Shaw, C. Schroeder *et al.*, "Staging of laser-plasma accelerators," *Phys. Plasmas* **23**, 056705 (2016).
- <sup>54</sup>M. Turner, A. Gonsalves, S. Bulanov, C. Benedetti, D. Terzani, J. van Tilborg, K. Nakamura, C. Schroeder, Z. Eisentraut, C. Geddes *et al.*, "BELLA petawatt second beamline commissioning and experimental plans," in *APS Division of Plasma Physics Meeting* (APS, 2021), Vol. 66.
- <sup>55</sup>K. Nakamura, L. Obst-Huebl, S. Hakimi, J. De Chant, Z. Kober, T. Ostermayr, S. Bulanov, A. Huebl, A. Gonsalves, C. Toth *et al.*, "IP2: High intensity experiment platform at the Bella petawatt laser," in *APS Division of Plasma Physics Meeting* (APS, 2021), Vol. 66.
- <sup>56</sup>P. L. Poole, A. Krygier, G. E. Cochran, P. Foster, G. Scott, L. Wilson, J. Bailey, N. Bourgeois, C. Hernandez-Gomez, D. Neely *et al.*, "Experiment and simulation of novel liquid crystal plasma mirrors for high contrast, intense laser pulses," *Sci. Rep.* **6**, 32041 (2016).
- <sup>57</sup>B. Shaw, S. Steinke, J. Van Tilborg, and W. P. Leemans, "Reflectance characterization of tape-based plasma mirrors," *Phys. Plasmas* **23**, 063118 (2016).
- <sup>58</sup>N. Czapla, D. Nasir, A. Zingale, D. Schumacher, L. Obst-Huebl, J. Bin, S. Steinke, K. Nakamura, A. Gonsalves, C. Geddes *et al.*, "High throughput and contrast enhancement from ultrathin liquid crystal films in a double plasma mirror configuration," in *APS Division of Plasma Physics Meeting* (APS, 2020), Vol. 65.
- <sup>59</sup>A. Gonsalves and A. Deshmukh, "GEECS (generalized equipment and experiment control system), version 00," No. 7314; 2014-003 (Lawrence Berkeley National Lab, 2017).
- <sup>60</sup>F. Nürnberg, M. Schollmeier, E. Brambrink, A. Blažević, D. Carroll, K. Flippo, D. Gautier, M. Geissel, K. Harres, B. Hegelich *et al.*, "Radiochromic film imaging spectroscopy of laser-accelerated proton beams," *Rev. Sci. Instrum.* **80**, 033301 (2009).
- <sup>61</sup>J. Bin, Q. Ji, P. Seidl, D. Raftrey, S. Steinke, A. Persaud, K. Nakamura, A. Gonsalves, W. P. Leemans, and T. Schenkel, "Absolute calibration of GafChromic film for very high flux laser driven ion beams," *Rev. Sci. Instrum.* **90**, 053301 (2019).
- <sup>62</sup>J. F. Ziegler, M. D. Ziegler, and J. P. Biersack, "SRIM—The stopping and range of ions in matter (2010)," *Nucl. Instrum. Methods Phys. Res., Sect. B* **268**, 1818–1823 (2010).
- <sup>63</sup>J. Perl, J. Shin, J. Schümann, B. Faddegon, and H. Paganetti, "TOPAS: An innovative proton Monte Carlo platform for research and clinical applications," *Med. Phys.* **39**, 6818–6837 (2012).
- <sup>64</sup>A. L. Palmer, A. Dimitriadis, A. Nisbet, and C. H. Clark, "Evaluation of Gafchromic EBT-XD film, with comparison to EBT3 film, and application in high dose radiotherapy verification," *Phys. Med. Biol.* **60**, 8741 (2015).
- <sup>65</sup>A. D. Piazza, C. Müller, K. Hatsagortsyan, and C. H. Keitel, "Extremely high-intensity laser interactions with fundamental quantum systems," *Rev. Mod. Phys.* **84**, 1177 (2012).
- <sup>66</sup>P. Zhang, S. S. Bulanov, D. Seipt, A. V. Arefiev, and A. G. R. Thomas, "Relativistic plasma physics in supercritical fields," *Phys. Plasmas* **27**, 050601 (2020).
- <sup>67</sup>A. Gonoskov, T. Blackburn, M. Marklund, and S. S. Bulanov, "Charged particle motion and radiation in strong electromagnetic fields," [arXiv:2107.02161](https://arxiv.org/abs/2107.02161) (2021).
- <sup>68</sup>A. Fedotov, A. Ilderton, F. Karbstein, B. King, D. Seipt, H. Taya, and G. Torgrimsson, "Advances in QED with intense background fields," [arXiv:2203.00019](https://arxiv.org/abs/2203.00019) (2022).
- <sup>69</sup>M. Tamburini, F. Pegoraro, A. D. Piazza, C. H. Keitel, and A. Macchi, "Radiation reaction effects on radiation pressure acceleration," *New J. Phys.* **12**, 123005 (2010).
- <sup>70</sup>M. Tamburini, F. Pegoraro, A. D. Piazza, C. H. Keitel, T. V. Liseykina, and A. Macchi, "Radiation reaction effects on electron nonlinear dynamics and ion

- acceleration in laser–solid interaction,” *Nucl. Instrum. Methods Phys. Res., Sect. A* **653**, 181–185 (2011).
- <sup>71</sup>M. Chen, A. Pukhov, T.-P. Yu, and Z.-M. Sheng, “Radiation reaction effects on ion acceleration in laser foil interaction,” *Plasma Phys. Controlled Fusion* **53**, 014004 (2010).
  - <sup>72</sup>L. Ji, A. Pukhov, and B. Shen, “Ion acceleration in the ‘dragging field’ of a light-pressure-driven piston,” *New J. Phys.* **16**, 063047 (2014).
  - <sup>73</sup>D. Wu, B. Qiao, and X. He, “The radiation reaction effects in the ultra-intense and ultra-short laser foil interaction regime,” *Phys. Plasmas* **22**, 093108 (2015).
  - <sup>74</sup>E. Nerush and I. Y. Kostyukov, “Laser-driven hole boring and gamma-ray emission in high-density plasmas,” *Plasma Phys. Controlled Fusion* **57**, 035007 (2015).
  - <sup>75</sup>W.-M. Wang, P. Gibbon, Z.-M. Sheng, Y.-T. Li, and J. Zhang, “Laser opacity in underdense preplasma of solid targets due to quantum electrodynamics effects,” *Phys. Rev. E* **96**, 013201 (2017).
  - <sup>76</sup>D. Del Sorbo, D. Blackman, R. Capdessus, K. Small, C. Slade-Lowther, W. Luo, M. Duff, A. Robinson, P. McKenna, Z. Sheng *et al.*, “Efficient ion acceleration and dense electron–positron plasma creation in ultra-high intensity laser–solid interactions,” *New J. Phys.* **20**, 033014 (2018).
  - <sup>77</sup>Y. Wu, L. Ji, L. Zhang, Z. Guo, B. Feng, X. Geng, Q. Yu, N. Wang, X. Zhang, B. Shen *et al.*, “Effects of radiation reaction on laser proton acceleration in the bubble regime,” *Phys. Plasmas* **25**, 093101 (2018).
  - <sup>78</sup>A. Samsonov, E. Nerush, and I. Y. Kostyukov, “Laser-driven vacuum breakdown waves,” *Sci. Rep.* **9**, 11133 (2019).
  - <sup>79</sup>M. Yano, A. Zhidkov, J. K. Koga, T. Hosokai, and R. Kodama, “Effects of hole-boring and relativistic transparency on particle acceleration in overdense plasma irradiated by short multi-pw laser pulses,” *Phys. Plasmas* **26**, 093108 (2019).
  - <sup>80</sup>C. Bula, K. McDonald, E. Prebys, C. Bamber, S. Boege, T. Kotseroglou, A. Melissinos, D. Meyerhofer, W. Ragg, D. Burke *et al.*, “Observation of nonlinear effects in Compton scattering,” *Phys. Rev. Lett.* **76**, 3116 (1996).
  - <sup>81</sup>D. Burke, R. Field, G. Horton-Smith, J. Spencer, D. Walz, S. Berridge, W. Bugg, K. Shmakov, A. Weidemann, C. Bula *et al.*, “Positron production in multiphoton light-by-light scattering,” *Phys. Rev. Lett.* **79**, 1626 (1997).
  - <sup>82</sup>J. Cole, K. Behm, E. Gerstmayr, T. Blackburn, J. Wood, C. Baird, M. J. Duff, C. Harvey, A. Ilderton, A. Joglekar *et al.*, “Experimental evidence of radiation reaction in the collision of a high-intensity laser pulse with a laser-wakefield accelerated electron beam,” *Phys. Rev. X* **8**, 011020 (2018).
  - <sup>83</sup>K. Poder, M. Tamburini, G. Sarri, A. D. Piazza, S. Kuschel, C. Baird, K. Behm, S. Bohlén, J. Cole, D. Corvan *et al.*, “Experimental signatures of the quantum nature of radiation reaction in the field of an ultraintense laser,” *Phys. Rev. X* **8**, 031004 (2018).
  - <sup>84</sup>H. Abramowicz, M. Altarelli, R. Aßmann, T. Behnke, Y. Benhammou, O. Borysov, M. Borysova, R. Brinkmann, F. Burkart, K. Büßer *et al.*, “Letter of intent for the LUXE experiment,” *arXiv:1909.00860* (2019).
  - <sup>85</sup>H. Abramowicz, U. Acosta, M. Altarelli, R. Assmann, Z. Bai, T. Behnke, Y. Benhammou, T. Blackburn, S. Boogert, O. Borysov *et al.*, “Conceptual design report for the LUXE experiment,” *Eur. Phys. J. Spec. Top.* **230**, 2445–2560 (2021).
  - <sup>86</sup>C. N. Danson, C. Haefner, J. Bromage, T. Butcher, J.-C. F. Chanteloup, E. A. Chowdhury, A. Galvanauskas, L. A. Gizzi, J. Hein, D. I. Hillier *et al.*, “Petawatt and exawatt class lasers worldwide,” *High Power Laser Sci. Eng.* **7**, e54 (2019).
  - <sup>87</sup>J. W. Yoon, Y. G. Kim, I. W. Choi, J. H. Sung, H. W. Lee, S. K. Lee, and C. H. Nam, “Realization of laser intensity over  $10^{23}$  W/cm<sup>2</sup>,” *Optica* **8**, 630–635 (2021).
  - <sup>88</sup>T. Nakamura, J. K. Koga, T. Z. Esirkepov, M. Kando, G. Korn, and S. V. Bulanov, “High-power  $\gamma$ -ray flash generation in ultraintense laser-plasma interactions,” *Phys. Rev. Lett.* **108**, 195001 (2012).
  - <sup>89</sup>C. Ridgers, C. S. Brady, R. Ducloux, J. Kirk, K. Bennett, T. Arber, A. Robinson, and A. Bell, “Dense electron-positron plasmas and ultraintense  $\gamma$  rays from laser-irradiated solids,” *Phys. Rev. Lett.* **108**, 165006 (2012).
  - <sup>90</sup>D. Stark, T. Toncian, and A. Arefiev, “Enhanced multi-MeV photon emission by a laser-driven electron beam in a self-generated magnetic field,” *Phys. Rev. Lett.* **116**, 185003 (2016).
  - <sup>91</sup>H. Rinderknecht, T. Wang, A. L. Garcia, G. Bruhaug, M. Wei, H. Quevedo, T. Ditmire, J. Williams, A. Haid, D. Doria *et al.*, “Relativistically transparent magnetic filaments: Scaling laws, initial results and prospects for strong-field QED studies,” *New J. Phys.* **23**, 095009 (2021).
  - <sup>92</sup>M. Borghesi, A. Schiavi, D. Campbell, M. Haines, O. Willi, A. MacKinnon, L. Gizzi, M. Galimberti, R. Clarke, and H. Ruhl, “Proton imaging: A diagnostic for inertial confinement fusion/fast ignitor studies,” *Plasma Phys. Controlled Fusion* **43**, A267 (2001).
  - <sup>93</sup>S. Göde, C. Rödel, K. Zeil, R. Mishra, M. Gauthier, F.-E. Brack, T. Kluge, M. MacDonald, J. Metzkes, L. Obst *et al.*, “Relativistic electron streaming instabilities modulate proton beams accelerated in laser-plasma interactions,” *Phys. Rev. Lett.* **118**, 194801 (2017).
  - <sup>94</sup>C. Palmer, J. Schreiber, S. Nagel, N. Dover, C. Bellei, F. Beg, S. Bott, R. Clarke, A. Dangor, S. Hassan *et al.*, “Rayleigh–Taylor instability of an ultrathin foil accelerated by the radiation pressure of an intense laser,” *Phys. Rev. Lett.* **108**, 225002 (2012).
  - <sup>95</sup>T. Ostermayr, C. Kreuzer, F. Englbrecht, J. Gebhard, J. Hartmann, A. Huebl, D. Haffa, P. Hilz, K. Parodi, J. Wenz *et al.*, “Laser-driven x-ray and proton micro-source and application to simultaneous single-shot bi-modal radiographic imaging,” *Nat. Commun.* **11**, 6174 (2020).
  - <sup>96</sup>A. Bienfait, J. Pla, Y. Kubo, X. Zhou, M. Stern, C. Lo, C. Weis, T. Schenkel, D. Vion, D. Esteve *et al.*, “Controlling spin relaxation with a cavity,” *Nature* **531**, 74–77 (2016).
  - <sup>97</sup>J. J. Barnard and T. Schenkel, “Modeling of intense pulsed ion beam heated masked targets for extreme materials characterization,” *J. Appl. Phys.* **122**, 195901 (2017).
  - <sup>98</sup>R. E. Lake, A. Persaud, C. Christian, E. S. Barnard, E. M. Chan, A. A. Bettiol, M. Tomut, C. Trautmann, and T. Schenkel, “Direct formation of nitrogen-vacancy centers in nitrogen doped compact transport systems for laser-driven proton beams,” *Appl. Phys. Lett.* **118**, 084002 (2021).
  - <sup>99</sup>J. De Chant, K. Nakamura, Q. Ji, L. Obst-Huebl, S. Barber, A. Snijders, T. Schenkel, J. van Tilborg, C. Geddes, C. Schroeder *et al.*, “Design optimization of permanent-magnet based compact transport systems for laser-driven proton beams,” in *APS Division of Plasma Physics Meeting (APS, 2021)*, Vol. 66.
  - <sup>100</sup>J.-L. Vay, A. Huebl, A. Almgren, L. Amorim, J. Bell, L. Fedeli, L. Ge, K. Gott, D. Grote, M. Hogan *et al.*, “Modeling of a chain of three plasma accelerator stages with the WarpX electromagnetic PIC code on GPUs,” *Phys. Plasmas* **28**, 023105 (2021).
  - <sup>101</sup>S. S. Bulanov, V. Y. Bychenkov, V. Chvykov, G. Kalinchenko, D. W. Litzenberg, T. Matsuoka, A. G. Thomas, L. Willingale, V. Yanovsky, K. Krushelnick *et al.*, “Generation of GeV protons from 1 PW laser interaction with near critical density targets,” *Phys. Plasmas* **17**, 043105 (2010).
  - <sup>102</sup>T. Nakamura, S. V. Bulanov, T. Z. Esirkepov, and M. Kando, “High-energy ions from near-critical density plasmas via magnetic vortex acceleration,” *Phys. Rev. Lett.* **105**, 135002 (2010).
  - <sup>103</sup>A. Pukhov and J. Meyer-ter Vehn, “Relativistic magnetic self-channeling of light in near-critical plasma: Three-dimensional particle-in-cell simulation,” *Phys. Rev. Lett.* **76**, 3975 (1996).
  - <sup>104</sup>L. D. Landau, J. Bell, M. Kearsley, L. Pitaevskii, E. Lifshitz, and J. Sykes, *Electrodynamics of Continuous Media* (Elsevier, 2013), Chap. 10.
  - <sup>105</sup>F. Sylla, M. Veltcheva, S. Kahaly, A. Flacco, and V. Malka, “Development and characterization of very dense submillimetric gas jets for laser-plasma interaction,” *Rev. Sci. Instrum.* **83**, 033507 (2012).
  - <sup>106</sup>J. Henares, P. Puyuelo-Valdes, F. Hannachi, T. Ceccotti, M. Ehret, F. Gobet, L. Lancia, J.-R. Marquès, J. Santos, M. Versteegen *et al.*, “Development of gas jet targets for laser-plasma experiments at near-critical density,” *Rev. Sci. Instrum.* **90**, 063302 (2019).
  - <sup>107</sup>J. D. Korablek, J. B. Kim, P. Brza, C. B. Curry, Z. Chen, H. A. Bechtel, A. A. Cordones, P. Sperling, S. Toleikis, J. F. Kern *et al.*, “Generation and characterization of ultrathin free-flowing liquid sheets,” *Nat. Commun.* **9**, 1353 (2018).
  - <sup>108</sup>I. Prencipe, A. Sgattoni, D. Dellasega, L. Fedeli, L. Cialfi, I. W. Choi, I. J. Kim, K. A. Janulewicz, K. Kakolee, H. W. Lee *et al.*, “Development of foam-based layered targets for laser-driven ion beam production,” *Plasma Phys. Controlled Fusion* **58**, 034019 (2016).
  - <sup>109</sup>M.-E. Manuel, B. Khair, G. Rigon, B. Albertazzi, S. Klein, F. Kroll, F.-E. Brack, T. Michel, P. Mabey, S. Pikuz *et al.*, “On the study of hydrodynamic

- instabilities in the presence of background magnetic fields in high-energy-density plasmas," *Matter Radiat. Extremes* **6**, 026904 (2021).
- <sup>110</sup>S. Hakimi, L. Obst-Huebl, A. Huebl, K. Nakamura, S. Bulanov, S. Steinke, W. Leemans, Z. Kober, T. Ostermayr, T. Schenkel *et al.* (2022). "Supplementary materials: Laser-solid interaction studies enabled by the new capabilities of the iP2 BELLA PW beamline," Zenodo. <https://doi.org/10.5281/zenodo.6050002>
- <sup>111</sup>S. S. Vazhkudai, B. R. De Supinski, A. S. Bland, A. Geist, J. Sexton, J. Kahle, C. J. Zimmer, S. Atchley, S. Oral, D. E. Maxwell *et al.*, "The design, deployment, and evaluation of the CORAL pre-exascale systems," in *SC18: International Conference for High Performance Computing, Networking, Storage and Analysis* (IEEE, 2018), pp. 661–672.
- <sup>112</sup>P. Hilz, T. Ostermayr, A. Huebl, V. Bagnoud, B. Borm, M. Bussmann, M. Gallei, J. Gebhard, D. Haffa, J. Hartmann *et al.*, "Isolated proton bunch acceleration by a petawatt laser pulse," *Nat. Commun.* **9**, 423 (2018).
- <sup>113</sup>J. Psikal, "Laser-driven ion acceleration from near-critical gaussian plasma density profile," *Plasma Phys. Controlled Fusion* **63**, 064002 (2021).
- <sup>114</sup>A. Sharma, "High energy electron and proton acceleration by circularly polarized laser pulse from near critical density hydrogen gas target," *Sci. Rep.* **8**, 2191 (2018).
- <sup>115</sup>A. R. Maier, N. M. Delbos, T. Eichner, L. Hübner, S. Jalas, L. Jeppe, S. W. Jolly, M. Kirchen, V. Leroux, P. Messner *et al.*, "Decoding sources of energy variability in a laser-plasma accelerator," *Phys. Rev. X* **10**, 031039 (2020).